The Astrophysical Journal, 613:159–179, 2004 September 20

COSMOLOGICAL FEEDBACK FROM HIGH-REDSHIFT DWARF GALAXIES

Akimi Fujita,[1,2,3] Mordecai-Mark Mac Low,[1,3] Andrea Ferrara,[4] and Avery Meiksin[5]

Received 2003 August 19; accepted 2004 May 27

ABSTRACT

We model how repeated supernova explosions in high-redshift dwarf starburst galaxies drive superbubbles and winds out of the galaxies. We compute the efficiencies of metal and mass ejection and energy transport from the galactic potentials, including the effect of cosmological infall of external gas. The starburst bubbles quickly blow out of small, high-redshift galactic disks, but must compete with the ram pressure of the infalling gas to escape into intergalactic space. We show that the assumed efficiency of the star formation rate dominates the bubble evolution and the metal, mass, and energy feedback efficiencies. With a star formation efficiency $f_* = 0.01$, the ram pressure of infall can confine the bubbles around high-redshift dwarf galaxies with circular velocities $v_c \gtrsim 52$ km s^{-1}. We can expect high metal and mass ejection efficiencies and moderate energy transport efficiencies in halos with $v_c \approx 30-50$ km s^{-1} and $f_* \approx 0.01$ as well as in halos with $v_c \approx 100$ km s^{-1} and $f_* \gg 0.01$. Such halos collapse successively from 1–2 σ peaks in ΛCDM Gaussian density perturbations as time progresses. These dwarf galaxies can probably enrich low- and high-density regions of intergalactic space with metals to 10^{-3} to 10^{-2} $Z_\odot$ as they collapse at $z \approx 8$ and $z \lesssim 5$, respectively. They also may be able to provide adequate turbulent energy to prevent the collapse of other nearby halos, as well as to significantly broaden Ly-α absorption lines to $v_{\rm rms} \approx 20-40$ km s^{-1}. We compute the timescales for the next starbursts if gas freely falls back after a starburst, and find that for star formation efficiencies as low as $f_* \lesssim 0.01$ the next starburst should occur in less than half the Hubble time at the collapse redshift. This suggests that episodic star formation may be ubiquitous in dwarf galaxies.

Subject headings: galaxies: dwarf — galaxies: evolution — galaxies: high-redshift — galaxies: starburst — hydrodynamics — shock waves

1. INTRODUCTION

1.1. *Overcooling and Angular Momentum Problems*

The theory of hierarchical structure formation in a universe dominated by cold dark matter (CDM) predicts that galaxies assembled from mergers of dark matter halos that gravitationally collapsed from primordial fluctuations. Within the same framework, the first luminous structures to form have subgalactic masses, given by the Jeans mass of the gas. This in turn is determined by the cooling mechanisms dominant during each cosmological era, since CDM models do not define a lower limit to the scale of inhomogeneities in the overall mass distribution. Protogalactic gas clouds of mass $M_h \sim 10^9$ $M_\odot$ begin to collapse as $\sim$3 σ peaks around redshift $z \sim 10$ and become dwarf galaxies.

The hierarchical scenario predicts the formation of numerous dwarf-sized halos at high redshift. In these halos, the dissipative collapse of gas is very efficient, since the cooling time $\tau \propto \rho^{-1} \propto (1+z)^{-3}$, where ρ is the mass density. This is often referred to as the overcooling problem (White & Rees 1978; White & Frenk 1991). Overcooling leads to a prediction of far more dwarf galaxies than observed, as well as to an angular momentum problem. When dense, cooled, protogalactic gas clouds or dwarf galaxies interact within a larger system such as the halo of a present-day disk galaxy, dynamical friction transfers their orbital angular momentum to the surrounding dark matter halo. The result is a galaxy with too much mass, rotating too slowly, and with angular momentum deficient by a factor of $\sim$25 relative to that observed (e.g., Katz & Gunn 1991; Navarro & Benz 1991; Navarro & White 1994).

Both of these problems can be resolved if a mechanism can be found to keep the gas diffuse until the peak of present-day disk (L_*) galaxy formation. Supernova feedback from young stars is one commonly invoked mechanism to do this. A number of cosmological hydrodynamic simulations have demonstrated that stellar feedback plays a major role in the formation of galaxies (Katz 1992; Navarro & White 1993; Yepes et al. 1997; Gerritsen & Icke 1997; Hultman & Pharasyn 1999; Scannapieco et al. 2001; Thacker & Couchman 2001; Sommer-Larsen et al. 2002; Springel & Hernquist 2003). However, the qualitative outcomes of simulations vary drastically with the feedback scheme applied. Recently, smoothed particle hydrodynamic (SPH) simulations by Scannapieco et al. (2001) and Springel & Hernquist (2003) show that overcooling in low-mass halos is significantly suppressed by the galactic outflows that they model, since the outflows slow down the accretion of gas in the halos and also strip baryons from neighboring halos (baryonic stripping). The latest high-resolution ($\sim 10^7$ h^{-1} $M_\odot$ per gas particle) SPH simulations by Thacker and Couchman (2001) and Sommer-Larsen et al. (2002) show that their treatment of thermal feedback with suppressed cooling succeeds in reproducing a present-day disk galaxy with angular momentum that is deficient only by a factor of a few.

However, these cosmological simulations still fail by orders of magnitude to resolve the physics of star formation and feedback. The coupling of feedback energy with interstellar gas through shocks, the formation of galactic outflows, and the coupling of the outflow energy with halo gas are not

---

[1] Astronomy Department, Columbia University, 550 West 120th Street, New York, NY 10027.

[2] Physics Department, University of California, Santa Barbara, CA 93109; fujita@physics.ucsb.edu.

[3] Astrophysics Department, American Museum of Natural History, Central Park West at 79th Street, New York, NY 10024-5192; mordecai@amnh.org.

[4] SISSA/International School for Advanced Studies, Via Beirut 4, 34014 Trieste, Italy; ferrara@arcetri.astro.it.

[5] Institute for Astronomy, University of Edinburgh, Blackford Hill, Edinburgh EH9 3HJ, UK; aam@roe.ac.uk.

physically represented, especially in SPH simulations with resolution at the galactic scale far too low to accurately resolve shocks. Therefore, it is important to model the collective action of multiple supernovae and study the formation of superbubbles and galactic winds in single dwarf galaxies, using high-resolution hydrodynamic simulations, in order to compute the feedback efficiencies (e.g., Mac Low & Ferrara 1999, hereafter MF99). Such models must also include a cosmological infall of gas at high redshift, because the ram pressure of the infall may influence the evolution of the superbubbles and galactic winds.

1.2. *Intergalactic Metals*

Observations of Lyα-absorbing clouds reveal the presence of metals. These clouds are thought to be regions of enhanced intergalactic medium (IGM) density distant from protogalaxies (see review by Rauch 1998). To transport metals into these regions, some mechanism, such as supernova-driven galactic outflows, must act. The observations show that Lyα forest clouds with neutral hydrogen column density with $\log N(\mathrm{H\,I}) > 14$ are metal enriched to $Z \approx 10^{-3}$ to $10^{-2}\ Z_{\odot}$ (Cowie et al. 1995; Songaila & Cowie 1996; Ellison et al. 2000), and that the metallicity remains roughly constant throughout the redshift range $1.5 < z < 5.5$ (Songaila 2001). It is also interesting to note that $\log N(\mathrm{H\,I}) \approx 14$ at $z \approx 3$ marks the transition between continuous filamentary structures and voids (e.g., Zhang et al. 1998).

The main candidates for the polluters of the IGM are starburst dwarf galaxies. The absence of turbulent motions observed in low-density Lyα clouds at $z \approx 3$ (Rauch et al. 2001b) suggests that metal enrichment was completed at very early times ($z \gg 5$), when the physical volume of the universe was smaller and contained the numerous dwarf galaxies predicted by the CDM model of galaxy formation (Rauch et al. 2001b; Madau et al. 2001; Scannapieco et al. 2002). On the other hand, the median Doppler parameters are significantly larger in the Lyα forest than predicted by cosmological simulations, suggesting some additional energy injection provided by late He II reionization or supernova-driven winds (Meiksin et al. 2001). In C IV systems with higher column densities, a substantial velocity scatter over length scales of a few hundred parsecs is observed, however, suggesting that they have been influenced by galactic feedback more recently (Rauch et al. 2001a; see Rauch 2002 for summary). Galactic outflows both at very high redshift and at lower redshift, $z \sim 3$, seem to play significant roles in enriching various regions of the IGM.

Cosmological simulations have suggested that the IGM at $z \approx 3$ can be metal enriched to $Z = 10^{-3}$ to $10^{-2}\ Z_{\odot}$ by the merging of or by outflows from dwarf galaxies (Gnedin 1998; Theuns et al. 2002; Thacker et al. 2002) without dynamically disturbing the observed low-density Lyα clouds. These simulations have the same problem as earlier: that the feedback schemes differ based on different assumptions about the coupling of supernova energy to the surroundings and the simulations fail badly to resolve star formation and the dynamics of bubbles.

1.3. *Starburst Wind Models*

The effects of repeated supernova explosions from starbursts appear to be a central piece of physics necessary for understanding the role of stellar feedback in both galaxy formation and IGM pollution. The effects of starbursts from dwarf galaxies on the surrounding interstellar medium (ISM) have been studied in the past both analytically and numerically (Mathews & Baker 1971; Larson 1974; Saito 1979; Dekel & Silk 1986; De Young & Heckman 1994; Silich & Tenorio-Tagle 1998; MF99; D'Ercole & Brighenti 1999). For example, MF99 studied the effects of repeated supernovae on local dwarf galaxies with gas mass $M_g = 10^6 - 10^9\ M_{\odot}$ using hydrodynamic simulations, and made a parameter study of mass and metal ejection efficiencies. The main results of MF99 are that mass loss is very inefficient except in the halos of lowest mass, while a substantial fraction of the hot, metal-enriched gas escapes from any of the potentials they studied. These results were confirmed by D'Ercole & Brighenti (1999) with a better treatment of thermal conduction. Recently, Mori et al. (2002) studied the same problem but in a spherical, nonrotating galaxy embedded in a halo with $M_h = 10^8\ h^{-1}\ M_{\odot}$ at $z = 9$. They find that with star formation efficiency $f_* = 0.1$, ~30% of the available supernova energy is transferred to the surrounding gas as kinetic energy. The starburst bubbles expand over $\gg 10\ R_v$, where R_v is the virial radius of the halo, comparable to the mean proper distance between neighboring low-mass systems. Their results support the suggestion that IGM metal enrichment occurs early. The recent study by Wada & Venkatesan (2003) improves on Mori et al. (2002) by precalculating a thin, dense disk with an inhomogeneous ISM in a given halo potential and by including self-gravity. They perform two three-dimensional models of a $10^8\ M_{\odot}$ galaxy with star formation efficiency $f_* = 0.14$ and 0.014 in our terms.

We follow the work of MF99 and extend their study to high redshift. Although the approaches taken by Mori et al. (2002) and Wada & Venkatesan (2003) are more realistic in some ways, the former neglects rotational flattening of the galaxy and both are far more expensive computationally. The MF99 approach enables us to do a parameter study on the feedback process by exploring a wide range of galaxy masses, formation redshifts, and star formation efficiencies. However, note that our study is limited to an axisymmetric geometry and also to single star formation sites at the centers of disks with a smooth ISM.

We perform careful, high-resolution models of the result of multiple supernova explosions in single dwarf galaxies at high redshift using the hydrodynamic code ZEUS-3D (Stone & Norman 1992; Clarke & Norman 1994) and compute the efficiency of metal and mass ejections and energy transport from the galactic potentials. We include the evolving dark matter halo potentials and the cosmological infall of halo gas computed with a one-dimensional hydrodynamic code (Meiksin 1994). The bubbles in MF99's local galaxies were solely governed by their interaction with the ISM, and so high metal ejection efficiencies were guaranteed once the bubbles blew out of the galactic disks. However, the bubbles in our high-redshift galaxies must still fight the ram pressure of the infalling halo gas after blowout before the metals, swept-up mass, and energy escape to intergalactic space. We also compute the accretion timescales for any mass swept up by the bubbles but bound by the potential to fall back to the center.

We model systems that we think likely to host a starburst. It is not certain whether first-generation systems were efficient in ejecting metals and transporting energy to the IGM, because an early cosmic UV background suppresses the formation of stars inside the systems by photodissociating their only cooling agent, molecular hydrogen (Haiman et al. 2000), or by raising the entropy floor (Oh & Haiman 2003). However, later systems that collapsed because of atomic hydrogen cooling may have been more robust, allowing starbursts to occur (Madau et al. 2001; Scannapieco et al. 2002; Oh & Haiman 2002).

We choose seven of these second generation systems, with $5 \times 10^8\ M_\odot \leq M_h \leq 5 \times 10^{10}\ M_\odot$ at $3 \leq z \leq 13$ and star formation efficiencies $f_* = 0.001$, 0.01, and 0.1. Our goal is to develop a generally useful description of supernova feedback in terms of metal ejection efficiencies $\xi_{\rm metal}$, mass ejection efficiencies ξ, and energy transport efficiencies ζ that can be widely used in large-scale cosmological simulations for the study of galaxy formation and metal enrichment. However, it will be shown in this paper that the parameterization of feedback is very difficult, and that we eventually need a higher resolution, adaptive mesh refinement, cosmological simulation with a realistic treatment of star formation to do so as reliably as we might wish. Nonetheless, we are able to reach several key conclusions with the present set of computations.

The paper is organized as follows. In § 2 we analytically predict the effects of ram pressure on the confinement of the starburst bubbles. In § 3 we discuss our numerical methods, including our models of cosmological infall (§ 3.1), starburst blowout (§ 3.2), and the tracer field we use to follow metal-enriched gas in the blowout model (§ 3.3). In § 4 we describe our choices for galaxy size (§ 4.1), disk model (§ 4.2), and star formation feedback (§ 4.3). We give our results in § 5: metal and mass ejection and energy transport efficiencies in § 5.1, the effects of external pressure on the bubble evolution in § 5.2, and the timescales for material to fall back in § 5.3. Our conclusions follow in § 6. Throughout the paper, we apply a ΛCDM cosmology with $\Omega_0 = 0.37$, $\Omega_\Lambda = 0.63$, $\Omega_b = 0.05$, $h = 0.7$, $\sigma_8 = 0.8$, and a primordial composition of H/He = 12/1.

2. PRESSURE CONFINEMENT

We first try to estimate analytically how the ram pressure of infalling gas affects the evolution of a starburst bubble, in order to estimate the ranges of halo mass M_h, redshift z, and star formation efficiency f_* over which the ram pressure confinement of a bubble suppresses feedback.

In this section, we consider a bubble in a power-law halo with gas density $\rho = \rho_0 r^{-\alpha}$. Isothermal halos with constant angular velocity have $\alpha = 2$. We take the bubble to be driven by a mechanical luminosity L_m for the 50 Myr lifetime of the least massive star able to go supernova after an instantaneous starburst and then to evolve freely thereafter. A bubble big enough to interact with the halo will blow out of the highly stratified exponential atmosphere of a high-redshift galactic disk very quickly. After it blows out, its evolution is largely determined by the infalling halo gas. Since the bubble accelerates as it blows out of the exponential ISM (Kompaneets 1960), it is difficult to exactly predict its expansion. Therefore, we make the simplifying assumption that the bubble has reached the power-law halo by 50 Myr, which is supported by our detailed numerical calculations, described in § 5. Thereafter, we compare the interior pressure of the bubble with the ram pressure of the infalling halo gas.

After the starburst ends at a time $t_f = 50$ Myr, the bubble continues to expand because of the residual energy of supernovae stored in the hot interior gas and in the shell. However, we do not know how much of the injected energy $L_m t_f$ remains in the interior, rather than being dissipated by radiative cooling enhanced by shell fragments mixing with the interior gas, and how much of it is transferred to the kinetic and thermal energy of the swept-up shell. Therefore, we assume a fraction ν of the injected energy $L_m t_f$ drives the bubble after t_f.

From the Rankine-Hugoniot jump conditions, we have

$$P = \frac{2}{\gamma + 1} \rho u_1^2, \tag{1}$$

where P is the pressure behind the shock front, $\rho = \rho_0 R_s^{-\alpha}$, the radius of the shock is R_s, and u_1 is the velocity ahead of the shock, in a frame of reference traveling with the shock velocity $\dot{R}_s$. The preshock velocity is

$$u_1 = \dot{R}_s + v_{\rm in}(R_s), \tag{2}$$

where the infall velocity of gas is $v_{\rm in}(R_s)$. We assume that the pressure P behind the shock equals the mean pressure $\bar{P}$ of the gas within the spherical volume enclosed by R_s, and a fraction ν of the total injected energy $L_m t_f$ gives the pressure (Spitzer 1978). (It is equivalent to setting $\zeta = 1$ in the Kompaneets approximation; however, in reality, it is not always true that $P = \bar{P}$: for example, $P \simeq 2\bar{P}$ in a Sedov blast wave solution; see Sedov 1959). We can then derive the shock velocity,

$$\dot{R}_s = 0.46 \left(\frac{\nu L_m t_f}{\rho_0} \right)^{1/2} R_s^{(\alpha - 3)/2} - v_{\rm in}(R_s), \tag{3}$$

where we have taken $\gamma = 5/3$ for an adiabatic bubble shock (but the coefficient varies by only 15% for a radiative shock with $\gamma = 1$) and we assume the thermal pressure of the IGM to be much smaller than its ram pressure. The shock velocity driven by the mechanical luminosity L_m prior to t_f exceeds that given by equation (3), but the bubble quickly decelerates without pressure support from the central energy source.

We approximate the infall velocity of gas,

$$v_{\rm in}(r) = (2GM_h/r)^{1/2}, \tag{4}$$

as that of a free fall onto a point mass with the mass M_h of the halo, as long as the radius r exceeds the virial radius R_v (given below by eq. [16]). We completely neglect the angular momentum of the infalling gas, so $v_{\rm in}$ is an upper limit. The bubble will stall when $\dot{R}_s = 0$ because of ram pressure exerted by the infalling gas. Thus, we can derive

$$v_{\rm in}(R_s) \geq 0.46 \left(\frac{\nu L_m t_f}{\rho_0} \right)^{1/2} R_s^{(\alpha - 3)/2} \tag{5}$$

as the criterion for ram pressure confinement. Both sides of the equation are functions of the bubble radius R_s, but we can eliminate the radial dependence in an isothermal halo with $\alpha = 2$ and compare both sides of the equation directly without knowing where the bubble is. Note that the left side of the equation is just under the escape velocity of a halo, $v_{\rm esc} \approx (GM_h/R_v)^{1/2}$ at $r \gtrsim R_v$, and the right side is the shock velocity of a bubble if there is no infalling gas.

The coefficient ρ_0 for the gas density of a spherically symmetric, power-law medium is

$$\rho_0 = M_h \left(\frac{\Omega_b}{\Omega_0} \right) \left(\frac{3 - \alpha}{4\pi} \right) R_v^{\alpha - 3}, \tag{6}$$

when a given total halo mass M_h is found within the virial radius R_v. The mechanical luminosity L_m can be expressed in terms of the star formation efficiency f_* as

$$L_m = \left(3.6\times10^{31}\ \mathrm{ergs\ s^{-1}}\right)\left(\frac{M_h}{M_\odot}\right)\left(\frac{f_*}{0.01}\right), \tag{7}$$

based on the Starburst99 model (Leitherer et al. 1999) described in § 4.

Substituting equations (4), (6), and (7) into equation (5) with $\alpha = 2$, we find that external ram pressure can confine a bubble at a given redshift z when the total halo mass

$$M_h \geq \left(8.3\times10^{9}\ M_\odot\right)\left(\frac{\nu f_*}{2\times10^{-3}}\right)^{3/2}\left(\frac{1+z}{9}\right)^{-3/2}. \tag{8}$$

We plot the above equation, the minimum halo mass for pressure confinement for different values of νf_*, in Figure 1. The starburst bubbles in the dwarf halos that we select for our study (*filled diamonds*: see § 4.1) are predicted to freely escape to intergalactic space if $f_* \gtrsim 0.1$ and to be completely confined by ram pressure of the infalling gas if $f_* \lesssim 0.001$ and $\nu \lesssim 0.5$. We discuss Figure 1 further in § 4.1. For a given νf_*, both the minimum halo mass for pressure confinement in equation (8) and the halo mass with a fixed virial temperature T_v or circular velocity v_c have the same redshift dependence, $M_h \propto (1+z)^{-3/2}$. Therefore, we can select a group of halos in which the ram pressure of the infall can confine the bubbles and so suppress the feedback efficiencies by a virial temperature or circular velocity cutoff: T_v^* or v_c^*. We cannot expect high feedback efficiencies in dwarf galaxies with

$$T_v \gtrsim T_v^* \simeq \left(1.0\times10^{5}\ \mathrm{K}\right)\left(\frac{\nu f_*}{1\times10^{-3}}\right),$$
$$v_c \gtrsim v_c^* \simeq \left(52\ \mathrm{km\ s^{-1}}\right)\left(\frac{\nu f_*}{1\times10^{-3}}\right)^{1/2}. \tag{9}$$

Without ram pressure from cosmological infall, a bubble will stall when its expansion is balanced by the thermal pressure of the IGM. If we follow the same procedure as above, we find that the bubble will only stall when its radius

$$R_s \gtrsim (10R_v)\left(\frac{\nu f_*}{1\times10^{-3}}\right)\left(\frac{T_{\mathrm{IGM}}}{2\times10^{4}\ \mathrm{K}}\right)^{-1}, \tag{10}$$

where we have assumed an ionized IGM.

The presence of ram pressure does generally appear to be important to the evolution of bubbles, and hence must be included when we compute the metal, mass, and energy feedback efficiencies in numerical simulations.

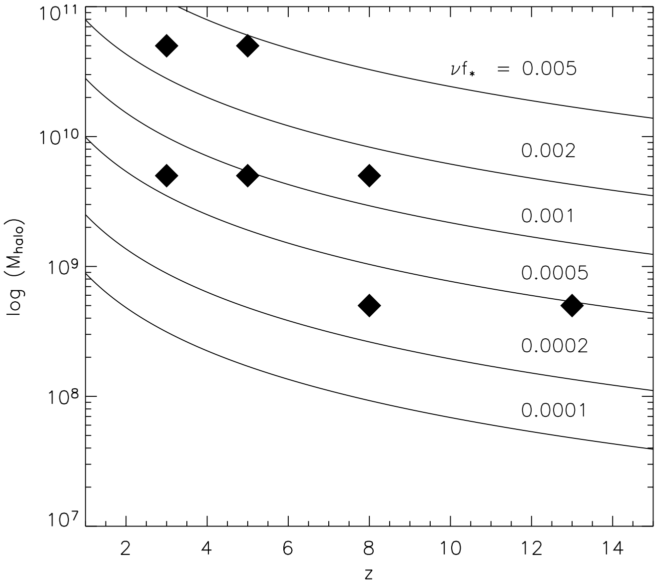

FIG. 1.—Plot of the minimum halo mass for ram pressure confinement of bubbles as a function of redshift for $0.0001 \leq \nu f_* \leq 0.005$, where the fraction of injected energy preserved in the bubbles is ν and the star formation efficiency is f_*. The galaxies we choose to model (described below in § 4.1) are shown as filled diamonds. The starburst bubbles in all our model galaxies are predicted to escape to intergalactic space if $\nu f_* \gtrsim 0.005$ and to be confined by ram pressure of the infalling gas if $\nu f_* \lesssim 0.0005$.

3. NUMERICAL METHODS

In this section, we outline the numerical methods we use to model feedback from dwarf galaxies. We first describe the model that we use for the evolution of the background halo, then the implementation of our models of starbursts. Finally, we examine an important detail of our model: the performance of the tracer field that we use to trace hot, metal-rich material from bubble interiors.

3.1. *Spherical Halo Model*

We model evolving dark matter halo potentials and the cosmological infall of gas onto them using a method based on the one-dimensional hydrodynamic computations of Meiksin (1994), which were developed to study the structure and evolution of Lyα clouds gravitationally confined by dark matter minihalos. The infall code described by Meiksin (1994) included standard CDM cosmology; we modified it for a flat ΛCDM cosmology. We neglect the effects of the repulsive force exerted by dark energy, since it is negligible at redshift $z \gtrsim 2$. This can be seen by considering the expansion parameter

$$H(t)^2 = [\dot{a}(t)/a(t)]^2 = 8\pi G\rho_M/3 + \Lambda/3, \tag{11}$$

where Λ is the cosmological constant and $\rho_M = (1.88\times10^{-29}\ h^2\ \mathrm{g\ cm^{-3}})\Omega_0(1+z)^3$. As z increases, matter dominates.

The infall code follows the evolution of spherical shells of dark matter based on a model of the spherical collapse of a Gaussian density perturbation (Bond et al. 1988). However, the dark matter shells are not allowed to interpenetrate as they collapse. Instead, each shell is brought to rest at its virial radius, building a halo that reflects the core structure of the initial perturbation, so the dark matter halo profile will not perfectly reproduce the results of N-body simulations, especially in the central regions. However, the central regions of the halo are less important anyway, because the disk of the galaxy dominates the potential in that region. As we discuss in § 4, we therefore include a separate disk term in the potential. The halo potential is more important for determining the density profile of the infalling gas at its edges, as well as capturing the details of the late evolution of the bubble as it climbs out of the potential well.

In the code, a linear Gaussian perturbation is evolved, starting at $z = 200$. For models that collapse at $z > 5$, we assume that the IGM is fully neutral with initial temperature $T_{\mathrm{bg}} = 550$ K, determined by the cosmic background radiation. For models that collapse at $z \leq 5$, we assume that H is ionized and He is singly ionized, with initial temperature $T_{\mathrm{bg}} = 10^4$ K, and we set the minimum temperature to which the gas is

TABLE 1

Model Galaxy Properties

z (1)	M_h ($M_\odot$) (2)	Resolution (pc) (3)	R_v (kpc) (4)	R_* (kpc) (5)	$T_{4,v}$ (10^4 K) (6)	H (pc) (7)	$v_{\rm esc}$ (km s^{-1}) (8)	v_c (km s^{-1}) (9)
13	5×10^8	2.7	1.6	0.17	4.7	35	48	37
8	5×10^8	5.2	2.5	0.27	2.0	74	40	29
	5×10^9	5.6	5.5	0.58	14.0	220	74	62
5	5×10^9	6.9	8.2	0.87	9.4	170	65	50
	5×10^{10}	15.0	18.0	1.9	43.0	360	130	110
3	5×10^9	10.0	12.0	1.3	6.2	400	52	41
	5×10^{10}	25.0	26.0	2.8	29.0	820	106	88

Note.—Col. (1): Redshift. Col. (2): Halo mass. Col. (3): Central zone size. Col. (4): Virial radius. Col. (5): Size of source region. Col. (6): Virial temperature. Col. (7): Scale height of galactic disk. Col. (8): Escape velocity. Col. (9): Circular velocity.

allowed to cool to be $T_{\rm min} = 10^4$ K. This very roughly captures the effects of UV background radiation after reionization, which actually heats the IGM to $\sim 2 \times 10^4$ K (Sargent et al. 1980).

We assumed that the reionization was completed at $z_{\rm ion} \sim 6$, and that the IGM was mostly neutral before $z_{\rm ion}$, based on the onset of the Gunn-Peterson trough against background quasars (Djorgovski et al. 2001; Becker et al. 2001). However, the recent measurement of a large electron-scattering optical depth by the *Wilkinson Microwave Anisotropy Probe* implies that a significant fraction of the IGM was already ionized by $z \sim 17 \pm 5$ (Kogut et al. 2003; Spergel et al. 2003). If our models at $z > 5$ are evolved in the reheated IGM instead, most of the gas ends up being pressure supported in halos with $T_v \approx 5 \times 10^4$ K and $v_c \approx 30$ km s^{-1}. However, the differences in density and pressure distributions appear only in central regions of the halos, where the gas cools to form disks. We discuss the effects of suppressed cooling in § 4.2.

The fluid equations are solved for baryons that cool by optically thin radiative recombination losses from H and He, dielectric recombination losses from He, bremsstrahlung, and Compton cooling from scattering off the microwave background. Cooling is turned off in the central region, where the potential is anyway unphysical, to avoid thermal instability. Collisional processes were included by Meiksin (1994) but were found to be unimportant outside of the accretion shock, so they have been neglected in our model to increase computational speed. We also neglect molecular hydrogen cooling.

The infall code produces a gas density distribution $\rho \propto r^{-\alpha}$, with $\alpha \approx 2-2.3$ for $r \lesssim R_v$ and $\alpha \lesssim 2$ outside, as predicted by the secondary infall model of Bertschinger (1985). The density distribution at the center is not correctly modeled by the infall code. However, we replace the central gas distribution with a rotationally supported disk, as described in the following section. The lack of cooling in the central region does produce shocks that convert some infall energy to thermal energy, and so the distribution of thermal or ram pressure alone is not well represented physically in our infall solutions, but the total pressure remains accurate. The details of the energy and velocity profiles ultimately depend on how gas is removed by the instabilities that make molecular clouds and stars, which we are still far from modeling.

Although we neglect the large-scale filamentary web predicted by three-dimensional hydrodynamic simulations, the spherical infall code is probably not too bad for the scale of our interest, because virialized systems form at the intersection of the filaments, where the accretion is more spherical within a scale on the order of the virial radius R_v, closely corresponding to minihalos (e.g., Miralda-Escude et al. 1996; Zhang et al. 1998). Adaptive mesh refinement simulations of first star formation by Abel et al. (1998, 2000, 2002) do show that gas accretion occurs along filaments, producing a highly structured, aspherical accretion shock even close to R_v. The results of our models in an idealized, spherical background can be interpreted as a *lower limit* to the effectiveness of metal, mass, and energy feedback, however, since a more dynamical, filamentary shape will always make it easier for galactic winds to find escape routes from dense regions.

3.2. *Starburst Models*

Our models of starburst blowout generally follow MF99 (see their § 4) and Fujita et al. (2003: see their § 4), so we briefly summarize our methods below.

We compute the evolution of the blast wave from starburst supernovae with ZEUS, an Eulerian, finite-difference, astrophysical gas dynamics code (Stone & Norman 1992; Clarke & Norman 1994) that uses second-order van Leer (1977) advection. We use a quadratic artificial viscosity to resolve shock fronts and a linear artificial viscosity to prevent instabilities due to strong shocks in standing flows. The former is necessary in any method that does not solve the Riemann problem, while the latter only acts at the zone-to-zone scale, and so does not affect larger scale features of the solutions. We use the loop-level parallelized version ZEUS-3D, in its two-dimensional form. Runs were done on Silicon Graphics Origin 2000 machines using eight processors, and typically took several days to a week, depending on the parameters of the galaxy.

We assume azimuthal symmetry around the rotational axis of the galaxy, and use a ratioed grid in both the radial and vertical directions to capture the multiple length scales of the problem. Our central, high-resolution grid extends to $\sim 0.5\ R_v$ and has typical zone sizes of a few parsecs at high redshift to a few tens of parsecs at lower redshift. Zone size increases by a factor of 10 across our ratioed grid but in the outer parts of the grid still remains under a few tens to hundreds of parsecs, respectively. The grids always capture several R_v. The actual values for the different models are listed in Table 1. The central resolution is high enough to resolve the stratified atmosphere of disks with more than 50 zones. This is found to yield converged results on the acceleration of bubbles, and is less than or at least equal to the typical size of a giant molecular cloud ($\sim$10–40 pc). We use reflecting boundary conditions along the symmetry axis and along the galaxy midplane and infall boundary conditions on the other two axes. The infall boundaries are fed by interpolation from intermediate results of the spherical collapse model described in the previous section.

To drive a constant-luminosity wind, we add mass and energy to a source region with a radius of five zones and a volume V. We choose the input rates based on the analytic solution by Weaver et al. (1977) for a constant density medium with density ρ_0 and energy e_0 of the center of the galactic disk. The energy density in each cell of the source zone is increased at a rate $\dot{e} = L_m/V$, where L_m is the mechanical luminosity from the starburst. The mass density is then increased at a rate $\dot{\rho} = \rho_0 \dot{e}/\eta e_0$ to roughly keep the specific energy of the source region constant.

The amount of mass in this wind accounts not only for supernova ejecta, but also mass that would have evaporated off the shells if we had included thermal conduction in our model. The evaporated mass does, in fact, dominate the mass within a realistic bubble (Weaver et al. 1977). Therefore, we add a larger amount of mass by choosing $\eta(L_m)$ for a given L_m, to reproduce the mass evaporation rate predicted by Weaver et al. (1977) for a spherical bubble. In this way, we keep the density and temperature within the superbubble fairly close to the analytic solution. See Fujita et al. (2003) for more details. With our choice of $\eta(L_m)$, the resulting interior temperature is always within a factor of 2 of the expected temperature.

We use a cooling curve for primordial gas in collisional ionization equilibrium (Sutherland & Dopita 1993) and also implement inverse Compton cooling appropriate for the high-redshift universe. We employ a sharp cutoff in the cooling at $T = 10^4$ K. This not only distinguishes ionized gas, which cools, from neutral gas, which does not cool at high redshift, but also mimics the effect of UV background radiation at intermediate redshift, in the absence of explicit models for photoionization and collisional ionization in our code. In the high-redshift, dense universe, we expect bubble shell shocks to be nearly isothermal because of efficient collisional cooling ($\Lambda_{\rm line} \propto n^2$), so the collisional ionization equilibrium cooling curve is a reasonable approximation. Strictly speaking, the assumption breaks down at the shock fronts, where underionization will increase the cooling rate, and in the evaporative flow off the shell, where overionization will decrease the cooling rate. Using the equilibrium curve overestimates cooling in the interiors, ensuring that our feedback efficiencies are lower limits to the true value.

The only place in the evolution of a bubble where substantial cooling occurs is in the dense, swept-up shell, where collisionally excited radiative cooling determines the density. The cooling in the shell does not directly affect the dynamical evolution of a bubble, which is controlled by the hot interior. The cooling timescale of the interior greatly exceeds the dynamical timescale of any realistic starburst bubble (Mac Low & McCray 1988). Instead, conductive and mechanical energy fluxes dominate its energy budget. Rayleigh-Taylor instability occurs when the shell begins to accelerate during blowout, so that the dense swept-up shell of ISM and halo gas is supported by the low-density, hot gas of thermalized supernova ejecta and evaporated shell gas inside.

The cooling curve is implemented in the energy equation in ZEUS-3D with a semi-implicit method. To solve the implicit energy equation, a Newton-Raphson root finder is used, supplemented by a binary search algorithm for occasional zones where the tabular nature of the cooling curve prevents the Newton-Raphson algorithm from converging. The empirical heating function from stellar energy input used in MF99 is turned off in our study, Instead, the sharp cutoff in the cooling function at $T = 10^4$ K prevents the background atmosphere from spontaneously cooling.

3.3. *Tracer Field and its Performance*

We use a tracer field, c, both to follow metal-enriched gas and to turn off radiative cooling in the hot bubble interior, in order to prevent mass numerically diffused off the dense shell from spuriously cooling the interior. The radiative cooling time of the interior is much longer than the dynamical time of the bubble for the galaxies of our study, so interior cooling is physically unimportant to the dynamics of the bubbles (Mac Low & McCray 1988). We set the cooling to be linearly proportional to the value of the tracer field, with the metal-enriched interior gas injected in the source region having $c = 0$; hereafter, we designate this as "colored" gas. We do not turn off Compton cooling in the bubble interior because it is only linearly dependent on the density.

We advect a function

$$f(c) = \tan[0.99\pi(c - 0.5)] \tag{12}$$

of the tracer field with exactly the same algorithm as the density, rather than the tracer field, c, itself, so that c will show a sharp transition at the interface even if $f(c)$ becomes quite smooth as the result of numerical diffusion (Yabe & Xiao 1993; MF99).

MF99 used the tracer field successfully to model modern, low-density dwarf galaxies, but we find that the bubbles in our high-redshift galaxies are severely poisoned by numerical diffusion, despite the sharpening of the edges by the tangent transform. Numerical diffusion occurs because of the failure in advection over a large density jump across a small number of zones.

The cooling time of the shells formed by initially adiabatic shocks is $t_c = 3kT_s/4n_0\Lambda(T_s)$, with a postshock electron number density $4n_0$ and shocked temperature $T_s = (3\mu_s/16k)v_s^2$, where μ_s is the mass per particle in the ionized ISM and v_s is shock velocity given by a similarity solution of a bubble in a uniform density medium n_0 by Weaver et al. (1977). We use the analytic estimate of the Gaetz & Salpeter (1983) cooling function between 10^5 and 10^7 K from Mac Low & McCray (1988),

$$\Lambda(T) = \left(1.0 \times 10^{-22}\ {\rm ergs\ cm^3\ s^{-1}}\right)\left(\frac{T}{10^6\ {\rm K}}\right)^{-0.7}\left(\frac{Z}{Z_\odot}\right). \tag{13}$$

This approximation agrees with the primordial cooling function of Sutherland & Dopita (1993) that we use for our simulations within a factor of a few in the temperature range. Then we find the instantaneous cooling time of the shocked ambient gas to be very short in the early, high-density universe,

$$\begin{aligned}\tau_s &= (0.19\ {\rm Myr}) L_{40}^{0.29} n_0^{-0.71} (Z/0.1\ Z_\odot)^{-1}\\ &\propto (1+z)^{-2.13}\end{aligned} \tag{14}$$

for a uniform density medium $n_0 \propto (1+z)^3$, so we expect the formation of dense shells with density $n \propto n_0\mathcal{M}^2$, where $\mathcal{M}$ is the Mach number.

We show the results of simple test simulations of the performance of the tracer field in Figure 2. Our standard model for this test has a fixed background density chosen at $z = 13$,

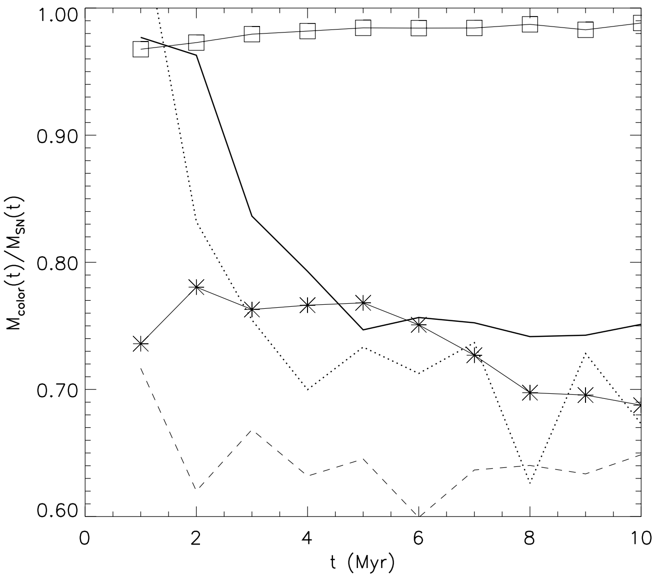

FIG. 2.—Fraction of mass tracked by the tracer field with $c < 0.6$, $M_{\rm color}(t)$ over the total mass injected with $c = 0$, $M_{\rm SN}(t)$ in our test simulations as a function of time up to 10 Myr. The results are based on a standard model at $z = 13$ with halo background density $\rho_{\rm bg} = 200\rho_0$, $L_m = 10^{40}$ ergs s^{-1}, primordial radiative cooling $\Lambda_{\rm line}$, and a resolution of 4 pc (*thick solid line*); the C100 model with extra cooling, $100\Lambda_{\rm line}$ (*solid line with stars*); the C0 model with no cooling (*solid line with squares*); the D10 model with the background density 10 times higher than the standard model (*dashed line*); and the LR model with zones 4 times larger than the standard model (*dotted line*). The tracer field fails to pick up some of the injected gas because of the unresolved, high-density shells at the contact discontinuity.

$\rho_{\rm bg} = 200\rho_0 = 2.5 \times 10^{-25}$ g cm^{-3}, which is an average halo gas density at that redshift, mechanical luminosity $L_m = 10^{40}$ ergs s^{-1}, and uses the primordial radiative cooling function by Sutherland & Dopita (1993). The zone size is 4 pc. We turned off Compton cooling for this test because it unnecessarily slows down the computation, but the degree of numerical diffusion that we find only becomes worse with the inclusion of Compton cooling.

With the standard model, the tracer field already fails to pick up 25% of initially marked interior gas by $t = 5$ Myr after the onset of starburst (at time step $\sim$5000). The same tracer field performs perfectly if the cooling is completely turned off (the adiabatic model, C0), while it does worse if the cooling strength is linearly increased by a factor of 100 (the extra cooling model, C100). The C0 model does so well because the adiabatic shell is fully resolved over $\sim$20 cells with density $\rho = 4 \times 200\rho_{\rm bg}$, while the isothermal shells are unresolved, with density $\rho \lesssim 200\rho_{\rm bg}\mathcal{M}^2$. As the cooling strength increases, the peak density approaches its theoretical prediction and the numerical diffusion gets worse. In the low-resolution simulation (LR) with 12 pc zones, the performance of the tracer field is even worse because of the failure to resolve the shell. Numerical diffusion increases in our models as unresolved, high-density, swept-up shells fragment after the bubbles blow out of the disks, increasing the area of contact between high- and low-density gas.

We find that the degree of numerical diffusion near unresolved shells does not improve substantially by changing the advection scheme from a second-order van Leer method to a third-order piecewise parabolic advection (PPA) method (Clarke & Norman 1994; Colella & Woodward 1984). We also find that changes in the size of source regions do not influence the performance of the tracer field.

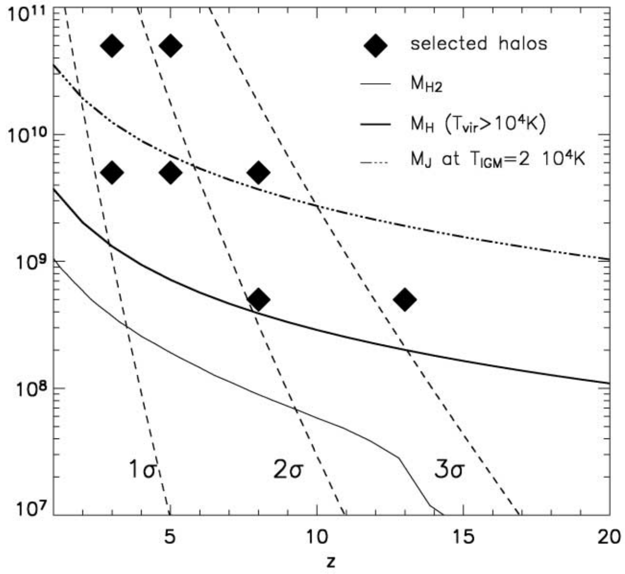

FIG. 3.—Seven second-generation systems (*filled diamonds*) with virial temperature $T_v > 10^4$ K (*thick solid line*). As a comparison, the minimum halo mass in which the gas can cool through molecular hydrogen is shown by the solid line, as computed by Tegmark et al. (1997) and given by B. Ciardi (2003, private communication). The Jeans mass after reionization is plotted by the triple-dot–dashed line. We also plot the halo mass expected to collapse from ΛCDM density perturbations as 1, 2, and 3 σ peaks (*dashed lines*).

The tracer field controls cooling, preventing it in gas marked as interior ejecta. When hot gas is mixed into regions colored as external, it is allowed to cool. As mass from the shell has usually numerically diffused into this gas, it cools unphysically quickly, so as diffusion proceeds the interior energy of the bubble is artificially dissipated. Our goal in this study is to compute metal and mass ejection and energy transport efficiencies by simulating the bubble dynamics in high-redshift galaxies with the tracer field. However, our simulations only yield strict lower limits on the efficiency of metal, mass, and energy feedback because of the numerical diffusion. To solve this problem we will eventually need either a high enough resolution to cleanly resolve shells, perhaps using adaptive mesh refinement, or else use of a true contact tracer, as in Mac Low et al. (1989).

4. GALAXY AND STAR FORMATION PARAMETERS

4.1. *Galaxies*

We model objects representing 1–3 σ peaks in the ΛCDM density perturbation spectrum (see Fig. 3). We focus on second-generation systems with virial temperature $T_v > 10^4$ K that can cool through line cooling by H and He. We show the galaxies we model with halo masses $M_h = 5 \times 10^8$–5×10^{10} $M_\odot$ that are expected to collapse at $z = 3, 5, 8$, and 13 in Figure 3. We make a list of the properties of our model galaxies in Table 1.

In these second-generation objects, the cooling time is much shorter than the dynamical time, so the gas will cool nearly isothermally at $\sim$$10^4$ K and rapidly flow to the centers. We assume that it settles in tightly bound, rotationally supported disks (Navarro & White 1994) without much fragmentation (Kashlinsky & Rees 1983; Oh & Haiman 2002). Such disks are mostly gravitationally stable, but a large fraction of out-of-equilibrium residual electrons expected during initial line cooling drives H_2 formation through gas-phase reactions catalyzed by H^- (Mac Low & Shull 1986; Shapiro & Kang 1987). Radiation from the H_2 allows the gas to cool further and collapse (Oh & Haiman 2002).

Figure 3 also shows the Jeans mass for gas in photoionization equilibrium with the background UV radiation with $T \approx 2 \times 10^4$ K. We chose two galaxies with $M_h = 5 \times 10^8\ M_\odot$ and $v_c \approx 30-40$ km s^{-1} at $z = 8$ and 13, assuming the effect of the UV background radiation to be negligible at $z > 6$. The cooling of gas in halos with $v_c \lesssim 30$ km s^{-1} is suppressed in the reheated IGM (e.g., Bond et al. 1988; Meiksin 1994; Efstathiou 1992; Thoul & Weinberg 1996). Therefore, we would not expect starbursts in such small halos at $z = 8$ if they are found in the IGM fully ionized by that time. The results in these halos should be interpreted in that light. We also chose three galaxies with $M_h = 5 \times 10^9\ M_\odot$ and $v_c \approx 40-60$ km s^{-1} at $z = 3$, 5, and 8. These galaxies fall below the Jeans mass, but hydrodynamic studies of dwarf halo formation show that $\sim$50% of baryons within the virial radius can still cool as long as $v_c \gtrsim 50$ km s^{-1} (Vedel et al. 1994; Thoul & Weinberg 1996; Navarro & Steinmetz 1997). We can still expect moderate starbursts in these halos.

As a comparison, we also plot in Figure 3 the minimum halo mass for first-generation, or Population III, systems with $T_v < 10^4$ K that can only cool through molecular hydrogen formation, as computed by Tegmark et al. (1997) for a standard CDM model. We do not select any of these first-generation objects because their star formation efficiency is expected to be very low because of the presence of internal and external photodissociating radiation (Omukai & Nishi 1999; Glover & Brand 2001; Haiman et al. 2000). We are far from realistically computing the efficiency of cooling and star formation even in second-generation systems that we study, and cannot definitively predict in which halos starbursts will occur at a given redshift. Instead, we perform a parameter study that explores a large range of dwarf galaxies to understand the physical processes of stellar feedback in different environments.

In Figure 1, we plot our chosen galaxies on top of the pressure confinement criterion given by equation (8) for different values of νf_*. With $f_* = 0.1$, equation (8) predicts that any bubble in a dwarf galaxy will escape to the IGM unimpeded by the ram pressure of infalling gas, unless the bubble has lost so much of its energy that $\nu < 0.1$ and the galaxy formed from an extremely large density perturbation (see Fig. 3). With $f_* = 0.001$, most second-generation systems with $T > 5 \times 10^4$ K are predicted to be confined by ram pressure with $\nu \leq 0.5$. The most interesting case in Figure 1 is that with $f_* = 0.01$. If the fraction of energy preserved in the bubbles $\nu \leq 0.2$, the bubbles in halos with $M_h \gtrsim 5 \times 10^{10}\ M_\odot$ from $\sim$2 σ peaks at $z = 3-5$ will be confined by the ram pressure of the infall. If $\nu \lesssim 0.1$, even bubbles in smaller halos with $M_h \approx 5 \times 10^9\ M_\odot$ will begin to be confined by the ram pressure. However, we can expect the bubbles in halos with $M_h \lesssim 10^9\ M_\odot$ ($T < 5 \times 10^4$ K) to escape to the IGM, unless most of their energy is lost to the surroundings. Figure 1 suggests high metal, mass, and energy feedback efficiencies in small high-redshift dwarf galaxies with $f_* = 0.01$ and in larger galaxies with $f_* \gg 0.01$. In § 5, we compare the results of our simulations with these predictions and try to constrain ν.

4.2. *Disks*

In our simulations, we set up a disk with a uniform surface density profile, $\Sigma = M_d/\pi R_*^2$, where R_* is the size of the disk, as in MF99. We choose a uniform surface density profile for numerical simplicity, although an exponential surface density distribution is observed in local blue compact dwarf galaxies (van Zee et al. 1998). However, bubble evolution is mainly governed by the vertical distribution of gas within the central region of the disk, where a constant surface density is a good approximation.

To compute the size of a galaxy as a function of halo mass and collapse redshift we follow Mo et al. (1998), using an isothermal halo profile. The size of a disk with a uniform surface density is

$$R_* = \frac{3}{\sqrt{2}} \left(\frac{j_d}{m_d} \right) \lambda R_v, \tag{15}$$

where R_v is the virial radius of a halo,

$$R_v = (16 \text{ kpc})(1+z)^{-1} \left(\frac{M_h}{10^9\ M_\odot} \right)^{1/3} (\Omega_0\ h^2)^{-1/3}, \tag{16}$$

where we use the same approximation for the ΛCDM model as in § 3.1 and we set the dimensionless spin parameter $\lambda = 0.05$, approximately at the peak of its distribution (e.g., Cole & Lacey 1996). We assume that a fraction of halo mass, $m_d = M_d/M_h$, settles into a non–self gravitating, rotationally supported disk in a singular isothermal halo with a fraction of the halo angular momentum, $j_d = J_d/J_h$. This method provides a good fit to the observed size distribution of galactic disks for $j_d/m_d = 1$ (Mo et al. 1998).

The baryonic content of each halo is $M_g = (\Omega_b/\Omega_0)M_h$, the amount of gas within the virial radius R_v if the gas simply follows the dark matter. We choose the mass that goes into the disk M_d by subtracting the result of the infall solution described in § 3.1 from M_g. Typically, $M_d \simeq 0.5 M_g$, but it varies by 10% among models with different cooling histories. The disks containing $\sim$50% of cooled baryons are appropriate for dwarf galaxies with $v_c \gtrsim 50$ km s^{-1}, but not for those with $v_c \approx 30$ km s^{-1} if the infall gas was initially reheated to a few $\times\, 10^4$ K (see § 4.1). In halos with $v_c \approx 30$ km s^{-1} at $z < z_{\rm ion}$, most of the halo is pressure supported and only small fractions of the gas mass M_g can cool to form disklike objects. The evolution of bubbles in such galaxies will only differ within the virial radius R_v from our standard models, with disk masses as high as $M_d \approx 0.5 M_g$. The qualitative results on metal, mass, and energy feedback efficiencies should not differ much, as long as disks or disklike objects with stratified ISM are assumed to form, because the bubbles blow out of them quickly to interact with the halo gas and the IGM. However, star formation efficiency f_* should be strictly $\lesssim$0.01 in the halos with $v_c \approx 30$ km s^{-1} if the collapse redshift $z < z_{\rm ion}$.

We initially set up the disk in hydrostatic equilibrium with a potential field due to the sum of the dark matter halo at the collapse redshift and the potential of a cold, thin disk representing earlier stars formed in fragmented gas or in the disk prior to any starburst. The dark matter potential computed by the infall code evolves as a function of time, but we do not modify the initial potential within R_v in our two-dimensional models. Since our dark matter profile is not realistic in the center, as discussed in § 3.1, we must include the cold, thin disk potential to model a disk with an exponential atmosphere that resembles the gas distribution observed in the Galaxy and nearby galaxies (Lockman et al. 1986; Neeser et al. 2002). To do so, we assume the presence of rather massive, thin disks containing $0.03 M_g$. This approximation of a fixed, cold disk potential is probably reasonable, since the dark matter still dominates the potential everywhere.

We assume that the gas in the disk is in the warm, neutral phase, with some turbulent contribution provided by winds and supernovae from the same small-scale star formation that formed the cold, thin disk, yielding an effective sound speed of $c_s \sim 10$ km s^{-1} with the corresponding temperature $T \approx 10^{3.7}$ K. Modeling this diffuse warm medium is important for the dynamics of bubbles, since the bubbles will immediately blow out of the cold gas disks where star formation is actually expected to occur (Mac Low & McCray 1988).

4.3. *Starbursts*

At the beginning of our simulations, we set up an instantaneous starburst at the center of each disk. The expansion of a starburst bubble can be considered to be an extension of superbubble dynamics in an OB association in a disk galaxy. The stellar winds create a hot, low-density cavity in the ISM, and repeated supernovae excavate a larger hole as they sweep the gas into a thin, dense shell (Tomisaka & Ikeuchi 1986; Mac Low & McCray 1988; Mac Low et al. 1989). Stellar winds are weaker in low-metallicity stars (e.g., Kudritzki 2002), but the initial few SNe will still create a similar hot cavity in high-redshift galaxies. Once the hot cavity forms, discrete supernova explosions generate blast waves that become subsonic in the hot interior, and hence can be treated as a continuous mechanical luminosity L_m in the study of bubble dynamics (Mac Low & McCray 1988).

It is of course an approximation to assume that all the mass available for the starburst turns into stars instantaneously and that the starburst is concentrated in a single spot at the center of a disk. Local observations of dwarf starburst galaxies show that multiple starburst clumps are scattered around the disks instead (e.g., Vacca 1996; Martin 1998). High-redshift disks are much smaller than present-day dwarf galaxies, roughly $R_* \propto (1+z)^{-1}$, but the smallest galaxy that we model extends over a few hundred pc, which is an order of magnitude larger than a typical molecular cloud ($\sim$10 pc). Therefore, we expect the same or at least similar starbursts in high-redshift galaxies also, as long as cooling is efficient. The starburst clumps are made up of OB associations or clusters. Since the largest OB associations or clusters have masses of a few million solar masses, we could actually think of our starbursts as being powered by a single star cluster as long as we do not assume too high a star formation efficiency in our model.

In our study, we use uniform mechanical luminosities computed using the Starburst99 model with $Z = 0.001$ (Leitherer et al. 1999). The Starburst99 model is based on a power-law initial mass function that approximates the classical Salpeter (1955) function, with exponent $\alpha = 2.35$ between low- and high-mass cutoff masses of 1 and 100 $M_\odot$, respectively. The average mechanical luminosity predicted by the Starburst99 model is $L_m = 2.7 \times 10^{40}$ ergs s^{-1} when $10^6\ M_\odot$ of gas is instantaneously converted to stars of mass between 1 and 100 $M_\odot$. Note that approximately the same mass of stars below 1 $M_\odot$ will form at the same time. The Starburst99 model is based on observations of star-forming and starburst regions in the local universe. However, various low- to intermediate-redshift observations suggest that the initial mass function may have been top heavy in the early universe (see the summary by Larson 1998), a suggestion supported by recent studies of Population III stars (Abel et al. 2000, 2002; Bromm et al. 1999, 2002; Nakamura & Umemura 1999, 2001). If the initial mass function is indeed top-heavy at high redshift, the fraction of O and B stars that contribute to the mechanical luminosity increases, so the conversion of the same amount of gas to stars can provide a higher mechanical luminosity than predicted by the Starburst99 model. Within the uncertainties, we assume that the mechanical luminosity of a burst is proportional to an amount of gas $f_* M_g$ available for a starburst as follows: $L_m = 2.7 \times 10^{40} f_* (M_g/10^6\ M_\odot)$ ergs s^{-1}.

Our mechanical luminosities range from $10^{39} < L_m < 10^{43}$ ergs s^{-1} produced when stars form from $(6-7) \times 10^4\ M_\odot$ of gas in the smallest halo with $f_* = 0.001$ and $(6-7) \times 10^8\ M_\odot$ in the largest halo with $f_* = 0.1$. These mechanical luminosities are equivalent to a supernova with an energy of 10^{51} ergs exploding every $\sim$17,000 yr to every $\sim$1.7 yr, respectively. Energy input is continued for a period of 50 Myr, roughly the lifetime of the smallest B star to go supernova (McCray & Kafatos 1987). Most cosmological simulations with supernova feedback employ $f_* \gtrsim 0.1$ to test its maximum effects.

We consider starburst efficiencies f_* in our galaxies of 0.001, 0.01, and 0.1. Numerical simulations of the first star formation suggest $f_* \approx 0.001$ in metal-free primordial clouds (Abel et al. 2000, 2002; Bromm et al. 1999, 2002). Oh & Haiman (2002) estimate an initial star formation efficiency by molecular hydrogen cooling alone to still be $f_* = 0.001$, even in second-generation disks. The star formation efficiency in such disks is not well constrained because of the presence of internal photodissociating UV radiation, but we can expect metal cooling to enhance the star formation efficiency if the halo gas is pre-enriched at least to $Z = 5 \times 10^{-4}\ Z_\odot$ by previous generations of stars (Bromm et al. 2001; Oh & Haiman 2002; Wada & Venkatesan 2003). Therefore, star formation could actually be rather efficient in second-generation objects. We think that $f_* \approx 0.01$ may be a reasonable guess for the initial major starburst in a galaxy. Starburst efficiencies as high as $f_* = 0.1$ are probably not realistic. Since we are performing a parameter study, however, we do consider them in order to clearly delineate the starburst efficiencies with which efficient metal and mass ejections and energy transport are expected in a halo at a given redshift.

5. RESULTS

We have explored the effects of repeated supernovae with mechanical luminosity linearly proportional to the amount of mass converted to stars, $f_* M_g$, in seven examples of early dwarf galaxies. Figure 4 shows the time histories of the density distributions of our model with $M_h = 5 \times 10^9\ M_\odot$ at $z = 8$, with starburst efficiencies f_* ranging from 0.001–0.1. The bubbles shown in Figure 4 are representative of our other models in a number of ways, as described below. (Figs. 5*a*–5*c* show the density distributions of all of our models at $t = 100$ Myr.)

The bubbles quickly begin to accelerate vertically through the stratified ISM of the galaxies, and blow out of the disks by $t \sim 10$ Myr after the onset of the starbursts. With sufficiently high central mechanical luminosity ($f_* = 0.01-0.1$), the bubbles sweep up the entire disks by $t = 30$ Myr. This behavior occurs in all of our galaxies because our high-redshift disks are very small, less than $\sim$1 kpc in size, and are highly stratified in their deep potential wells. Most of the ISM remains bound, so these disks are not yet "blown away" in the sense used by De Young & Heckman (1994) and MF99. In fact, we show below that most of the ISM remains bound to the halo potentials if $f_* \lesssim 0.01$.

The internal termination shocks outside the freely expanding winds and ejecta are clearly seen at $t = 10-30$ Myr,

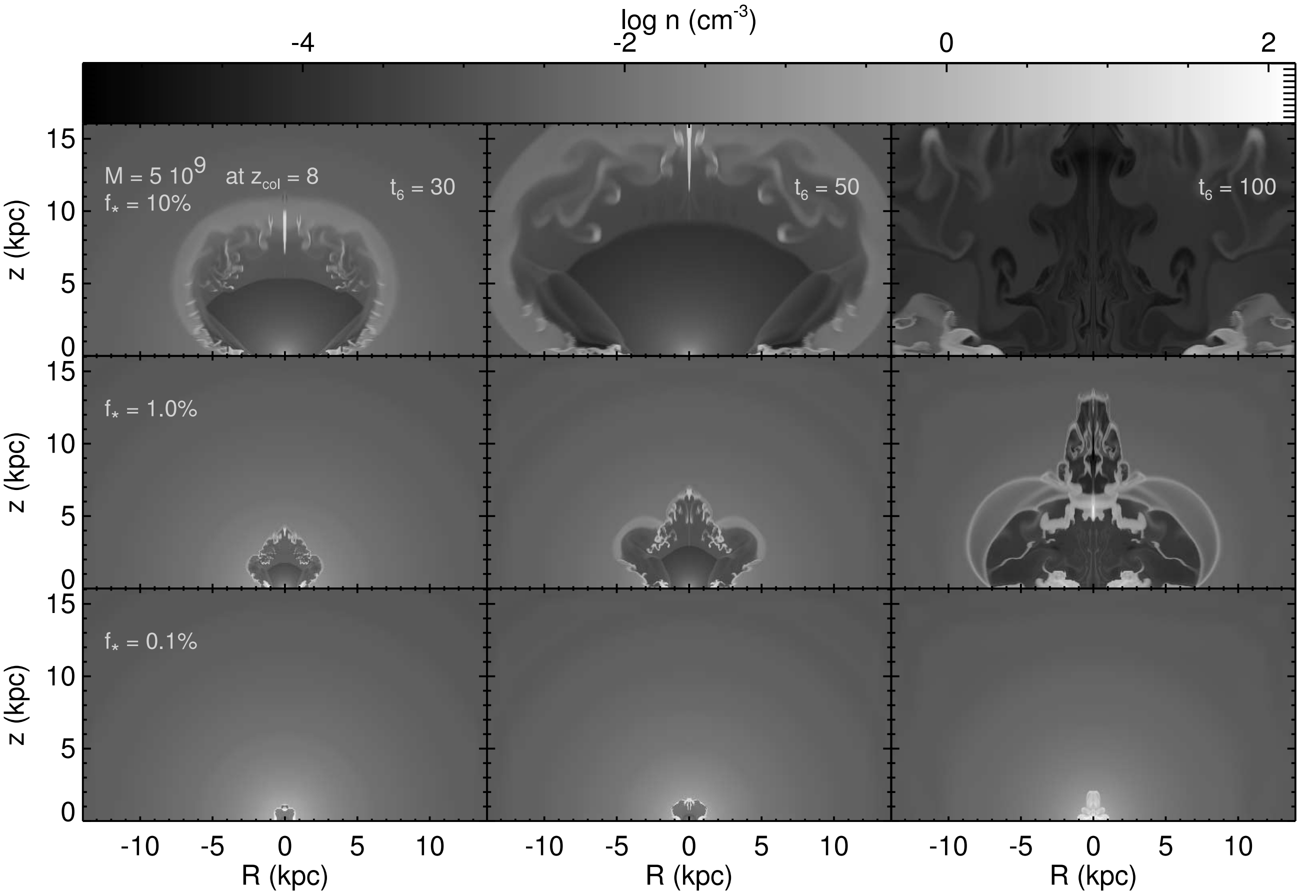

Fig. 4.—Density distributions for our model with halo mass $M_h = 5 \times 10^9\ M_\odot$ at $z = 8$ are shown at times 30 Myr (*left*), 50 Myr (*middle*), and 100 Myr (*right*) after the onsets of starbursts with star formation efficiencies $f_* = 0.1\%$ (*bottom*), 1% (*middle*), and 10% (*top*). Corresponding mechanical luminosites are $L_m = 1.8 \times 10^{39}$, 1.8×10^{40}, and 1.8×10^{41} ergs s^{-1}, respectively.

surrounded by hot, pressurized regions of shocked winds and supernova ejecta. The hot, pressurized regions drive shocks into the surrounding ISM and halo gas, sweeping it up. In these high-redshift dense galaxies, gas behind the outer shocks tends to cool efficiently, so that the shocks are usually isothermal. Outside the galactic disks, the shocks are no longer isothermal. Figure 6 shows the formation of dense shells, cooled from $T_s \approx 10^5$ K, driven by the hot, pressurized gas at $T \approx 10^7$ K behind, as the bubble blows out of the disk at $t = 10$ Myr, with $f_* = 0.01$ (middle panel in Fig. 4). The swept-up gas forms dense, cold, thin shells, except in the cases where $f_* = 0.1$, in which the shocks are so fast that cooling remains inefficient.

Shell formation is extremely sensitive to the resolution employed, and is not fully resolved in our simulations (see Fig. 6 and the resolution study of shell formation in Fujita et al. 2003). Resolving the shell is not important in following the overall dynamical evolution of bubbles driven by the thermal energy of the hot pressurized regions (Castor et al. 1975; Weaver et al. 1977), but is important to follow the details of shell fragmentation due to Rayleigh-Taylor instability when the bubbles accelerate. Figure 4 shows examples of shell fragmentation. The development of the Rayleigh-Taylor instability in our model is limited not only by the resolution, but also by the assumption of an azimuthal symmetry. Mac Low et al. (1989) pointed out that in an axisymmetric blowout, the typical spike and bubble structure of the Rayleigh-Taylor instability is limited to rings. Thus, the detailed structure of the fragments will be different in three dimensions. However, the instabilities seen in our simulations effectively allow hot gas to accelerate beyond the cold, swept-up shells, which is the qualitative result of interest. Figure 4 shows that for $f_* \geq 0.01$ the hot, metal-enriched gas expands into the IGM well beyond the virial radius of the halo, leaving behind the fragmented shells, which eventually fall back into the center. The hot gas is confined in the vicinity of the disk if $f_* = 0.001$. Similar behavior can be seen in Figures 5*a*–5*c* for all of our model galaxies.

We now discuss our quantitative results. We compute metal and gas ejection and energy transport efficiencies in § 5.1; discuss the effects of external ram pressure from infalling gas on the evolution of the bubbles and thus on the feedback efficiencies in § 5.2; and estimate in § 5.3 how long it takes for swept-up but still bound mass to fall back to the center of a halo, where it will be available to fuel the next starburst.

5.1. *Feedback Parameters*

In order to quantify feedback, we measure metal ejection efficiency $\xi_{\rm met}$, mass ejection efficiency ξ, and energy transport efficiency ζ. In each case, we measure the content of gas that has been accelerated to outward velocities higher than the local escape velocity defined by the gravitational potential. Because of the limitations of our model, we actually measure the efficiencies when the bubbles reach $2R_v$, where we assume the low-density IGM to begin. This choice is rather arbitrary,

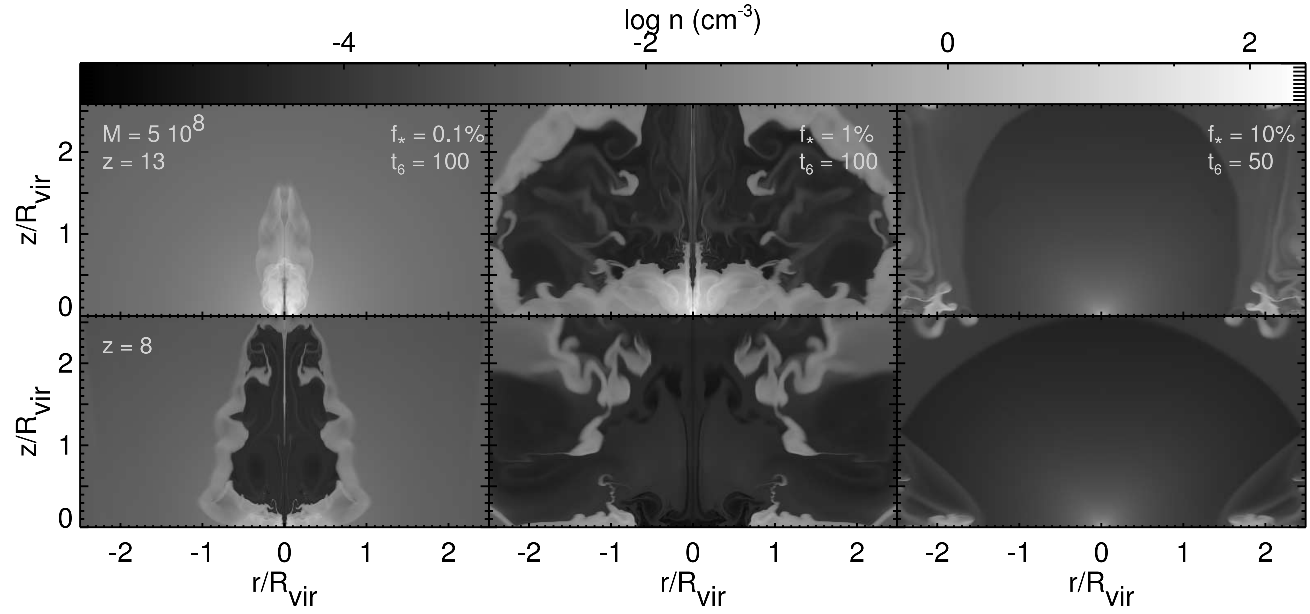

FIG. 5*a*

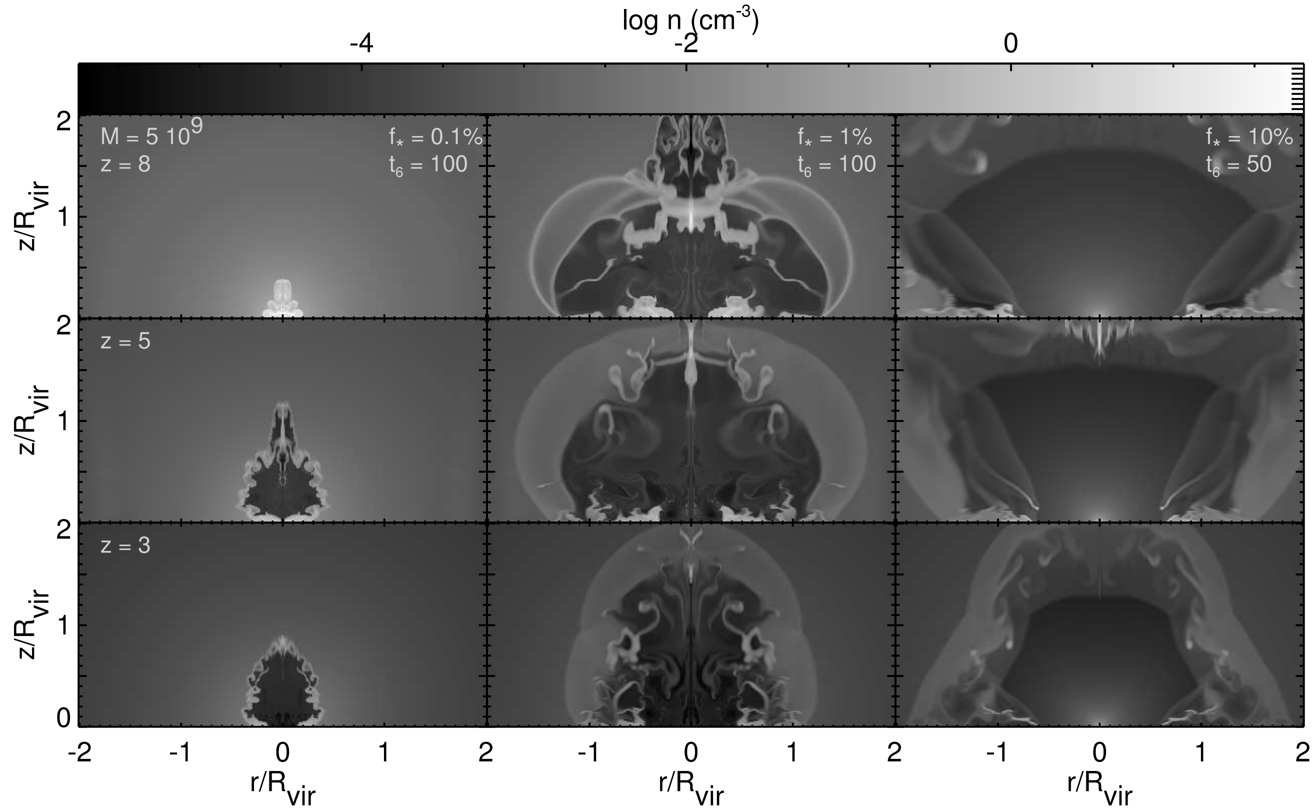

FIG. 5*b*

FIG. 5.—Density distributions at $t = 100$ Myr for $f_* = 0.1\%$ (*left*) and 1% (*middle*) and at $t = 50$ Myr for $f_* = 10\%$ (*right*) for models with halo mass (*a*) $M_h = 5 \times 10^8\ M_\odot$ at $z = 13$ and 8; (*b*) $M_h = 5 \times 10^9\ M_\odot$ at $z = 8$, 5, and 3; and (*c*) $M_h = 5 \times 10^{10}\ M_\odot$ at $z = 5$ and 3.

and is only motivated by the idea that the bubble should be well outside the halo virial radius R_v in order to see the effect of the ram pressure of infalling gas.

Recall that we use a one-dimensional, spherical background potential (§ 3.1). Simulations show that filamentary structures are anchored in spheroidal halos (Zhang et al. 1998). Thus, the spheroidal approximation is a good one within a virial radius, but becomes progressively worse beyond. In reality, bubbles such as those we model would possibly find their way out to low-density regions between the filaments. When the bubble finds such a funnel for escape, we expect that any gas carrying supernova energy and metals that has velocity greater than the escape velocity of the halo potential will escape nearly unimpeded into the IGM.

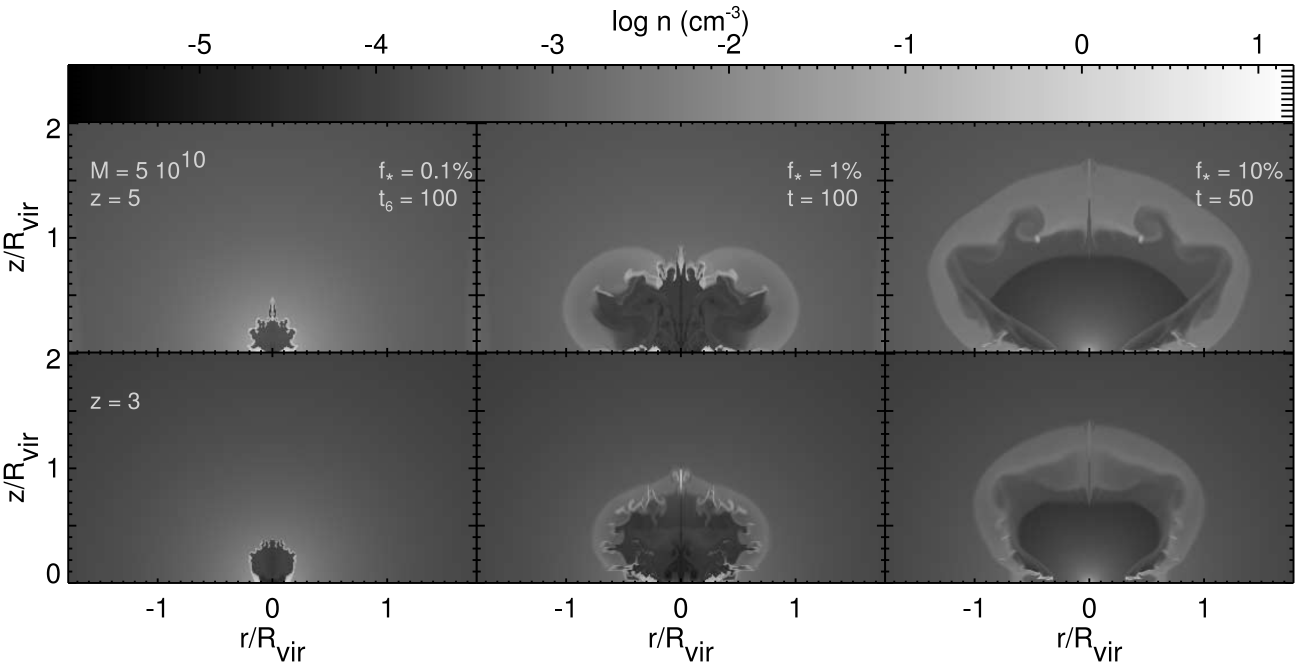

FIG. 5*c*

5.1.1. *Metal Ejection Efficiency*

The metal ejection efficiency was defined by MF99 as

$$\xi_{\mathrm{met,\,MF}} = M_{c,\,\mathrm{esc}}/M_{\mathrm{SN}}, \tag{17}$$

where $M_{c,\,\mathrm{esc}}$ is the mass of metal-enriched gas moving with a speed greater than the local escape velocity and colored by a tracer field with $c < 0.6$, and M_{SN} is the total mass injected at the center with $c = 0$ initially, which accounts not only for winds and supernova ejecta but also for the mass evaporated off the swept-up shell by thermal conduction. The colored mass, M_c, traced is not sensitive to the choice of the cutoff number (0.6) in the absence of numerical diffusion. The mass M_{SN} is found inside the hot, pressurized region in which metals are assumed to be mixed well. Equation (17) is based on the assumption that the injected mass, M_{SN}, is preserved at the time of its measurement without being mixed into the ambient medium physically or numerically. However, the numerical diffusion severely poisons the colored gas as discussed in § 3.3, and our tracer field only picks up ~60% of originally colored gas within 5–10 Myr after the onset of the starbursts.

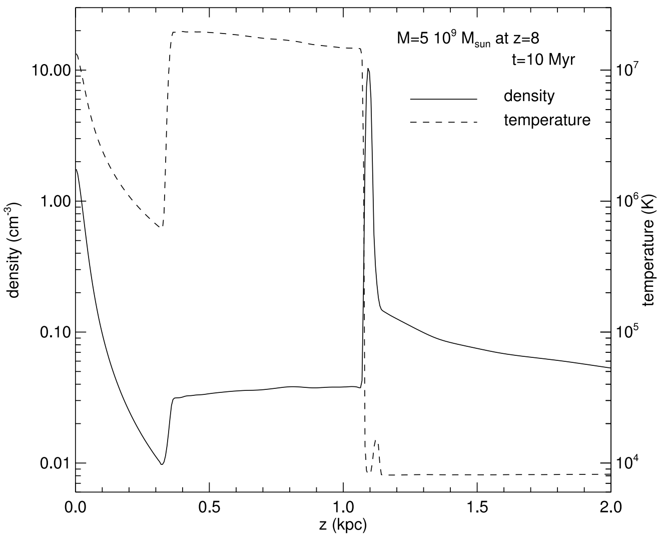

FIG. 6.—Density and temperature distributions of the bubble in the disk with $M = 5 \times 10^9$ $M_\odot$ at redshift 8, at $t = 10$ Myr after the onset of starburst with $f_* = 0.01$. We plot them through the vertical z-direction from the galactic center.

At the same time, we observe a significant amount of physical mixing between the metal-enriched colored gas and the ambient gas. We show in Figure 7 an example of metal mixing inside a bubble in a halo with $M_h = 5 \times 10^8$ $M_\odot$ at $z = 8$. The dense, swept-up shell of ambient gas fragments because of Rayleigh-Taylor instability when the bubble blows out at $t \approx 10$ Myr. Figure 7 shows the density distribution of the bubble at $t = 19$ Myr, and shows that the fragmented shells mix with the hot interior gas very effectively. This physical mixing of gas accelerates numerical diffusion further. Unfortunately, we have no systematic way of tracking physical metal mixing, nor of distinguishing it from numerical diffusion, but it is important to quantify the fraction of the escaping gas enriched with metals to any extent.

Therefore, it is not appropriate for us to use equation (17), since we severely underestimate the metal ejection efficiencies when we cannot track down the total amount of originally colored mass. Instead, we define the metal ejection efficiency as

$$\xi_{\mathrm{met}} = M_{c,\,\mathrm{esc}}/M_c, \tag{18}$$

where now the color cutoff $c < 1 - \epsilon$, with ϵ chosen to be small. In this way, we are sure to pick up any metal-enriched gas (that is, gas that was injected with $c = 0$) and still obtain a strong lower limit to the actual metal ejection rate, since $M_c \gg M_{\mathrm{SN}}$. Figure 8 shows the colored mass M_c as a function of ϵ for the halo with $M_h = 5 \times 10^8$ $M_\odot$ at $z = 8$ for star

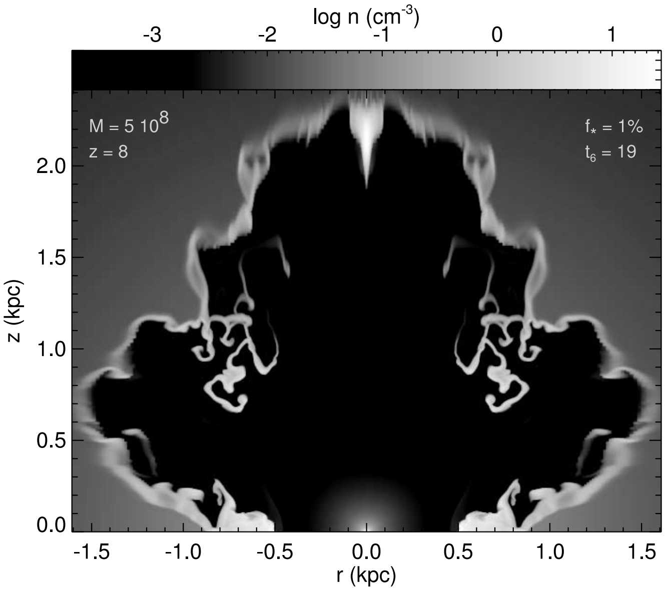

FIG. 7.—Density distribution of model with halo mass $M_h = 5 \times 10^8\ M_\odot$ at $z = 8$, immediately after the bubble blows out of the disk at $t = 19$ Myr with $f_* = 1\%$. The simulation was run with a resolution of 2.6 pc within the central 1 kpc^2, decreasing smoothly to 26 pc beyond $r \approx z \approx 2$ kpc. The cooled, swept-up shell of ambient gas fragments because of Rayleigh-Taylor instability, and mixes with the hot, low-density interior gas very effectively.

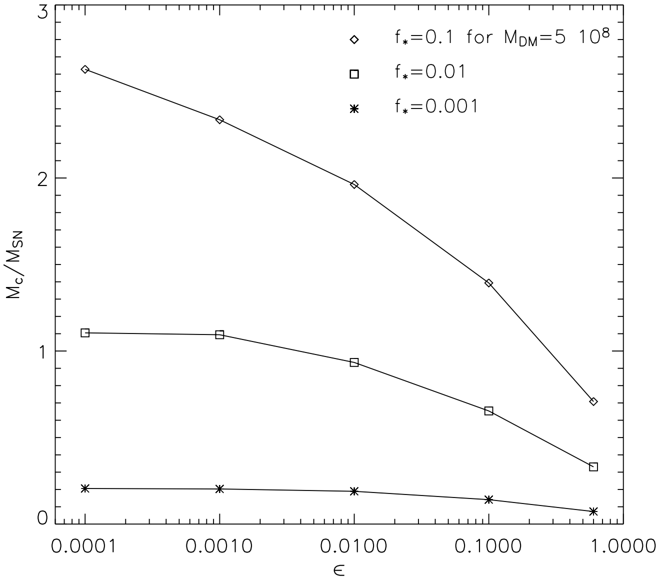

FIG. 8.—Colored mass, M_c, divided by the total colored mass injected with $c = 1 M_{\rm SN}$ as a function of $\epsilon = 1 - c$ for the halo with $M_h = 5 \times 10^8\ M_\odot$ at $z = 8$ for star formation efficiencies $f_* = 0.001$, 0.01, and 0.1. The masses M_c were measured when the bubbles reached $2R_v$ at $t = 100$ Myr when $f_* = 0.001$ and 0.01 and at $t = 50$ Myr when $f_* = 0.1$. The values of M_c are insensitive to the choices of ϵ as long as they are very small, except for the case with $f_* = 0.1$ because it was measured at an earlier time.

formation efficiencies $f_* = 0.001, 0.01$, and 0.1. The masses M_c were measured when the bubbles reached $2R_v$ at $t = 100$ Myr when $f_* = 0.001$ and 0.01 and at $t = 50$ Myr when $f_* = 0.1$. The mixing between the colored gas and the ambient gas proceeded far by $t = 100$ Myr for the bubbles with $f_* = 0.001$ and 0.01 (see Fig. 5*a*), so the values of M_c are insensitive to the choices of ϵ as long as they are very small. The asymptotic value of M_c as ϵ decreases is not reached for the case with $f_* = 0.1$, because it was measured at an earlier time. However, the bubble is so powerful as to reach $2R_v$ by that time, so any values of M_c will yield $\xi_{\rm met} \approx 1$ with $10^{-4} \leq \epsilon \leq 0.6$. We choose $\epsilon \approx 10^{-4}$ to 10^{-3} to enforce $M_c < M_g$, the total mass of baryons in the halo.

The metal ejection efficiencies, $\xi_{\rm met}$, are nearly zero in all the halos that we study when the star formation efficiency $f_* = 0.001$, and close to 1 with $f_* = 0.1$ (Table 2). These results are consistent with our prediction in § 2 that in the presence of infall ram pressure, the bubbles in second-generation objects can escape to the IGM if $f_* = 0.1$ but will be confined within the halo potentials if $f_* = 0.001$ and $\nu \lesssim 0.5$. We find that the metal ejection efficiencies are largely determined by the value of f_* that we assume. Recall that $f_* = 0.1$ is likely to be unrealistic for an instantaneous starburst in second-generation systems.

The most interesting results are therefore the values of $\xi_{\rm met}$ with $f_* = 0.01$. Metal ejection efficiencies are low in halos with $M_h = 5 \times 10^{10}\ M_\odot$ at $z = 3$ and 5 and even with $M_h = 5 \times 10^9\ M_\odot$ at $z = 8$. However, high metal ejection efficiencies $\xi_{\rm met} \gtrsim 0.5$ occur in halos with virial temperatures $T_v \lesssim 1 \times 10^5$ K or circular velocities $v_c \lesssim 50$ km s^{-1} at all redshifts we studied. These galaxies may make significant contributions to the metal-enrichment of the IGM. On the other hand, larger galaxies with $v_c \approx 100$ km s^{-1} allow efficient cooling, so star formation efficiencies $f_* \gg 0.01$ may be plausible. These galaxies could then produce and expel more metals to the IGM.

If we assume that each supernova produces $\sim 3\ M_\odot$ of heavy elements (Ferrara & Tolstoy 2000), a halo with dynamical mass M_h can expel metals with mass

$$M_{\rm met} \approx (8 \times 10^4\ M_\odot)\left(\frac{\xi_{\rm met}}{0.5}\right)\left(\frac{f_*}{0.01}\right) \times \left(\frac{M_h}{5 \times 10^8\ M_\odot}\right). \tag{19}$$

If we further assume that those metals mix uniformly, we can estimate the average metallicity of the universe from halos at a given redshift z:

$$\bar{Z} \simeq (6 \times 10^{-4}\ Z_\odot) \times \int_{M_{\rm min}(z)}^{M_{\rm max}} \left[\frac{N_h(M_h, z)\, dM_h}{1\ {\rm Mpc}^{-3}}\right]\left[\frac{\xi_{\rm met}(M_h, z)}{0.5}\right] \times \left[\frac{f_*(M_h, z)}{0.01}\right]\left(\frac{M_h}{5 \times 10^8\ M_\odot}\right), \tag{20}$$

where $N_h(M_h, z)dM_h$ is the comoving number density of halos at z with masses between M_h and $M_h + dM_h$, predicted from Press-Schechter theory (Press & Schechter 1974; Bond et al. 1991) in our ΛCDM model, and $M_{\rm max}$ and $M_{\rm min}(z)$ are the maximum and minimum halo masses to be incorporated into the calculation. We set $M_{\rm min}(z) = 5.8 \times 10^8\ M_\odot[(1+z)/9]^{-3/2}$, corresponding to $v_c = 30$ km s^{-1}. Although the metals may well be distributed highly inhomogeneously, equation (20) provides a lower limit to the average metallicity of intergalactic clouds where the expelled metals can reach.

Assuming $\xi_{\rm met} f_*$ to be constant, we plot the average metallicity $\bar{Z} \propto \xi_{\rm met} f_*$ (eq. [20]) as a function of mass $M_{\rm max}$ at $z = 3$, 5, 8, and 13 in Figure 9. We chose $\xi_{\rm met} f_* = 0.005$, which means, for example, $f_* = 0.01$ and $\xi_{\rm met} = 0.5$ for halos with $v_c \approx 50$ km s^{-1}, and $f_* = 0.05$ and $\xi_{\rm met} = 0.1$ for halos

TABLE 2

METAL AND MASS EJECTION AND ENERGY TRANSPORT EFFICIENCIES

z (1)	M_h ($M_\odot$) (2)	f_* (3)	$\xi_{\rm met}$ (4)	ξ (5)	ζ (6)	Blow Away (7)
13.........	5×10^8	0.1	0.99	3.2	0.45	Yes
	5×10^8	0.01	0.68	0.33	0.17	No
	5×10^8	0.001	0.0	0.0	0.0	No
8...........	5×10^8	0.1	0.99	4.5	0.76	Yes
	5×10^8	0.01	0.64	1.1	0.34	No
	5×10^8	0.001	0.15	0.026	5.5×10^{-4}	No
	5×10^9	0.1	1.0	1.7	0.48	Yes
	5×10^9	0.01	0.03	0.0088	0.024	No
	5×10^9	0.001	0.0	0.0	0.0	No
5...........	5×10^9	0.1	1.0	1.8	0.80	Yes
	5×10^9	0.01	0.44	0.30	0.069	No
	5×10^9	0.001	0.0	0.0	0.0	No
3...........	5×10^9	0.1	1.0	1.7	0.92	Yes
	5×10^9	0.01	0.88	0.99	0.18	Yes
	5×10^9	0.001	0.0	0.0	0.0	No
5...........	5×10^{10}	0.1	1.0	0.86	0.73	No
	5×10^{10}	0.01	0.0	0.0	0.0	No
	5×10^{10}	0.001	0.0	0.0	0.0	No
3...........	5×10^{10}	0.1	1.0	1.2	0.75	Yes
	5×10^{10}	0.01	0.0	0.0	0.0	No
	5×10^{10}	0.001	0.0	0.0	0.0	No

NOTE.—Col. (1): Redshift. Col. (2): Halo mass. Col. (3): Star formation efficiency. Col. (4): Metal ejection efficiency. Col. (5): Mass ejection efficiency. Col. (6): Energy transport efficiency. Col. (7): Whether more than half of ISM has been blown away from galactic potential.

with $v_c \approx 100$ km s^{-1}. Although we neglect the dependence of $\xi_{\rm met}$ on halo properties for a given f_*, Figure 9 shows a qualitative trend of metal contributions from halos at different redshifts.

In Figure 9, the metal contribution seems to be poor from halos at $z = 13$ but rather substantial from halos at $z = 8$. The average metallicity at $z = 8$ from halos with $v_c \lesssim 50$ km s^{-1} alone is already approaching $\bar{Z} \approx 10^{-3}\ Z_\odot$, the lower limit of the metallicity observed in low-density Lyα clouds at $z \approx 3-5.5$. Such halos correspond to $\sim$2 σ peaks in our ΛCDM primordial density perturbations. The early enrichment at $z \approx 8$ may explain the absence of kinematic disturbance observed in low-density Lyα clouds at $z \approx 3$ (Rauch et al. 2001b; Madau et al. 2001), by which time the kinematic effects of the wind may have dissipated and the gas resettled onto the filaments. Note, however, that the metal contributions from halos $v_c \lesssim 50$ km s^{-1} are a factor of a few larger at lower redshifts, since they are more abundant (1–2 σ peaks) with larger halo masses and so can produce more metals with the same $\xi_{\rm met} f_*$.

Figure 9 also shows that the larger galaxies with $v_c \approx 100$ km s^{-1} begin to make significant contributions, yielding $\bar{Z} \gtrsim 10^{-2}\ Z_\odot$ at $z \approx 3-5$. The high H I column density Lyα clouds ($\log N_{\rm H\,I} > 14.4$) with $Z \approx 10^{-2}\ Z_\odot$ (Cowie et al. 1995) might have been recently enriched by such dwarf galaxies then. This picture of recent enrichment is also supported by the large turbulent motions ($v_{\rm rms} \approx 70$ km s^{-1}) observed in high column density C IV systems (Rauch et al. 2001b).

Our estimates in Figure 9, based on our numerical simulations, suggest that both dwarf starburst galaxies with $v_c \approx 30-50$ km s^{-1} and those with $v_c \approx 100$ km s^{-1} can be very efficient in spreading metals, but to different regions of the IGM (low- and high-density clouds) at different times ($z \approx 8$ and $z \lesssim 5$). We find that only galaxies collapsing from 1–2 σ peaks are abundant enough to make significant contributions to the metal enrichment of the IGM.

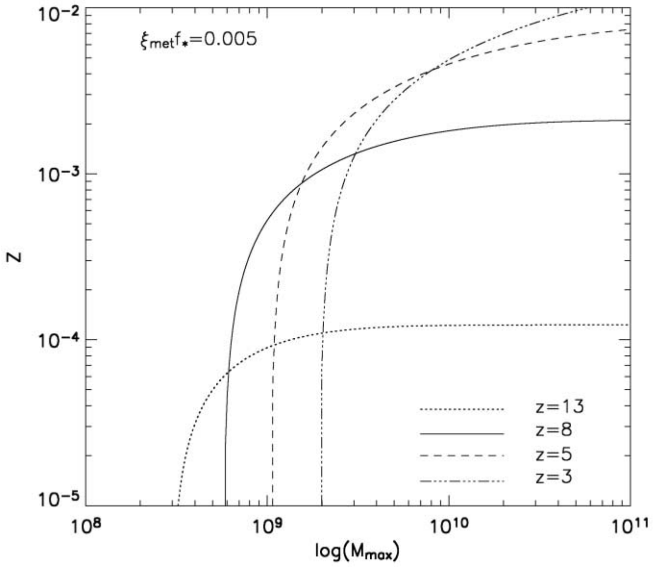

FIG. 9.—Average metallicity of the universe, $\bar{Z}$, from halos with mass between $M_{\rm min}(z)$ and $M_{\rm max}$ at redshifts, 3, 5, 8, and 13 for $\xi_{\rm met} f_* = 0.005$.

Metal ejection efficiencies $\xi_{m,\rm MF} \sim 1$ were found by MF99 in all of the local dwarf galaxies that they modeled, even with star formation efficiency $f_* = 0.001$, while we found negligible metal feedback with $f_* = 0.001$ in high-redshift galaxies. We showed in § 5.2 that the difference between our results and those of MF99 is not the higher densities $\rho \propto (1 + z)^3$, because bubbles quickly blow out of the smaller disks, with smaller scale heights expected at higher redshift. Rather, it is the ram pressure from cosmological infall that makes the difference.

5.1.2. *Gas Mass Ejection Efficiency*

We define the efficiency of gas mass ejection as

$$\xi = \frac{M_{\rm esc}}{(\Omega_b/\Omega_0)M_h}, \tag{21}$$

where $M_{\rm esc}$ is the mass moving with velocity $v \geq v_{\rm esc}$ and the denominator is the mass of baryons initially within R_v, since we assumed they initially simply follow the dark matter in our models. We list ξ for each of our models in Table 2.

The mass $M_{c,\rm esc}$ of escaping, metal-enriched gas is a negligible fraction of $M_{\rm esc}$. The bulk of the mass escaping is some combination of the ISM and infalling halo gas. Since we do not systematically track the disk gas in our simulations, we identify gas with angular momentum as disk gas, although there is some transfer of angular momentum between the disk and ambient gas because of numerical diffusion and physical mixing. Our accuracy is limited, so we can only observe whether $\gtrsim$50% of the ISM is moving faster than the escape velocity or not. Halos in which this occurs are marked as having had their ISM blown away in Table 2.

Table 2 shows that the mass ejection efficiencies $\xi \gtrsim 1$ with $f_* = 0.1$ and are nearly zero with $f_* = 0.001$, consistent with the metal ejection efficiencies. More than half of the disk gas escapes the potentials when $f_* = 0.1$ in all the halos except one. Blow away is possible with $f_* = 0.1$ because high-redshift galaxies are very small and easily swept away by powerful bubbles; however, our result should be interpreted carefully because of our assumption of an instantaneous starburst at a single site (see the discussion in § 4.3). With $f_* = 0.01$, the mass ejection efficiencies ξ can be large for the same parameters when $\xi_{\rm met}$ is large, but most of the escaping mass is from the halo, while the ISM remains bound. (This agrees with MF99 and D'Ercole & Brighenti 1999, who found that ISM loss is inefficient so long as it is distributed nonspherically.)

Thus, a substantial fraction of infalling halo gas can acquire enough energy from the bubbles to escape the potentials. For example, halo gas mass comparable to $(\Omega_b/\Omega_0)M_h$ escapes from the halo potentials with $M_h = 5 \times 10^8\ M_\odot$ at $z = 8$ and $M_h = 5 \times 10^9\ M_\odot$ at $z = 3$, even with $f_* = 0.01$. These results have two interesting implications for galaxy formation: further cooling in the halos can be suppressed to a certain degree, which we discuss in § 5.3; and the turned-around halo gas will carry the energy of supernova explosions to other sites of halo formation, perhaps preventing their collapse, which we discuss next.

5.1.3. *Energy Transport Efficiencies*

In order to compute the energy transport efficiency ζ, we add up the kinetic energy K and thermal energy U carried by any gas with $v > v_{\rm esc}$, subtracting the potential energy required to escape the local potential well:

$$\zeta = \frac{K_{\rm esc} + U_{\rm esc} - [\Phi(2R_v) - \Phi(r)]}{L_m t_f}, \qquad (22)$$

where $\Phi(r)$ is the potential of a gas parcel located at r, $\Phi(2R_v)$ is the potential at $2R_v$ from the center, and the input energy is $L_m t_f$. We exclude thermal energy carried by any swept-up shell of ISM material and infalling gas if the Hubble time at a given redshift $t_{\rm H}(z)$ exceeds the cooling time of a shell with radius $R_{\rm shell}$,

$$\tau_s = (78{,}000\ {\rm yr})\left(\frac{1+z}{9}\right)^{-3}\left[\left(\frac{\nu}{0.2}\right)\left(\frac{f_*}{0.01}\right)\right]^{1.7} \times \left[\frac{R_{\rm shell}}{R_v(M_h, z)}\right]^{0.3}\left(\frac{Z}{Z_\odot}\right)^{-1}, \qquad (23)$$

where we assume that the density profile is that of an isothermal halo (eq. [6]), the bubble is driven by the residual energy $\nu L_m t_f$ with star formation efficiency f_*, and R_v is the virial radius for a given halo M_h at a given redshift z. We used equation (13) for the cooling rate $\Lambda(T)$. In fact, $\tau_s \ll t_{\rm H}(z)$ unless $f_* = 0.1$ at $z \leq 8$.

We cannot systematically distinguish between energy carried by hot, metal-enriched gas and swept-up, ambient gas because of numerical diffusion. However, we can safely compute the amount of thermal energy carried by escaping shells of swept-up gas with a conservative color cutoff, $c > 0.6$, because the thermal energy is carried by the gas that is recently shock heated and therefore not mixed with ejecta by numerical diffusion. In Figure 10, we plot the fractions of energy carried by ejecta and by ambient gas with $c > 0.6$ in a halo with $M_h = 5 \times 10^9\ M_\odot$ at $z = 3$. It shows that swept-up halo gas carries most of the energy, in kinetic form. Even if we raise the color cutoff to $c > 1 - \epsilon$, the kinetic energy of the ambient gas remains much larger than that of the interior gas. After the bubble blows out at $t \approx 10$ Myr, the thermal energy of the hot interior is effectively transferred to the surrounding gas. The bubble reaches $2R_v$ by $t \simeq 100$ Myr, and the fraction of energy escaping $\zeta \approx 0.18$. Energy transport efficiencies ζ for all the models are listed in Table 2.

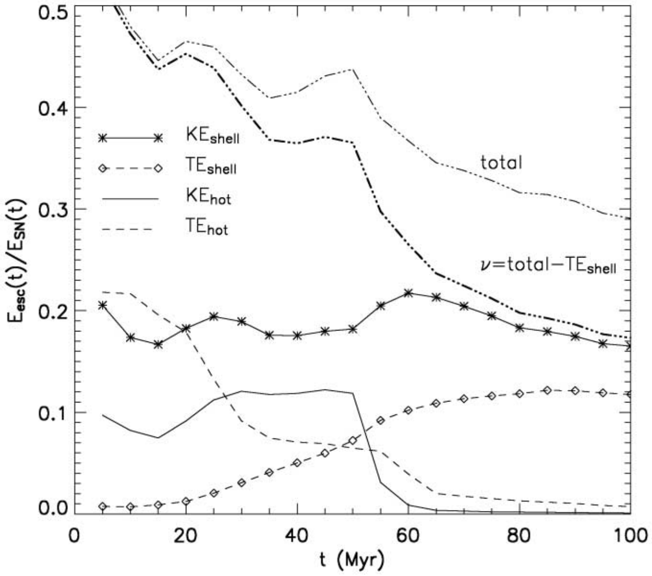

FIG. 10.—Fractions of total injected energy escaping from the potential with $M_h = 5 \times 10^9\ M_\odot$ at $z = 3$: total energy escaping (*thin triple-dot–dashed line*); total energy excluding thermal energy carried by swept-up gas liable to be radiated, defined as ν (*thick triple-dot–dashed line*); kinetic energy (*solid line with stars*) and thermal energy (*dashed line with diamonds*) carried by swept-up halo gas; and kinetic energy (*solid line*) and thermal energy (*dashed line*) carried by hot interior gas with the tracer $c < 0.6$.

We note that numerical diffusion could accelerate the cooling of the bubbles. However, a resolution study of energy in models with $f_* = 0.01$ and $M_h = 5 \times 10^8\ M_\odot$ at $z = 8$ using standard and doubled resolution shows no more than 30% differences in energy (Fig. 11). The largest differences are in shell thermal energy, which is least affected by numerical diffusion. This suggests that the dissipation of bubble energy seen in our simulations is physical, not dominated by numerical diffusion.

The transfer of the blast wave energy into the IGM is effective, with $\zeta \rightarrow 1$, in models with $f_* = 0.1$ and negligible if $f_* = 0.001$, as expected from our discussion of the metal and mass ejection efficiencies. The energy transport efficiencies ζ are roughly proportional to the mass ejection efficiencies ξ, because the escaping mass is carrying most of the energy. Both seem to be largely determined by f_*. With $f_* = 0.01$, the energy transport efficiencies are $\zeta \sim 0.1$–0.3 in halos with $v_c \lesssim 50$ km s^{-1}. Larger halos with $v_c \approx 100$ km s^{-1} have more efficient cooling, and therefore are likely to have higher star formation efficiencies, $f_* \gg 0.01$, so that they can transport more total energy into the IGM.

This kinetic energy feedback could stir intergalactic gas and support it against gravitational collapse in other halos. Recent numerical work has demonstrated that supersonic turbulence can delay gravitational collapse for many free-fall times in turbulent molecular clouds (Gammie & Ostriker 1996; Klessen et al. 2000). However, turbulent energy decays quickly, in a time roughly proportional to the crossing time, $t_{\rm cr} = L/v_{\rm rms}$, of a turbulent region of size L with a flow of rms velocity $v_{\rm rms}$ (Mac Low 1999; Elmegreen 2000). The distance reached by the turbulent motions is only $\sim L\sqrt{2}$ after half the energy is lost at $t_{\rm cr}$ (Avila-Reese & Vázquez-Semadeni 2001).

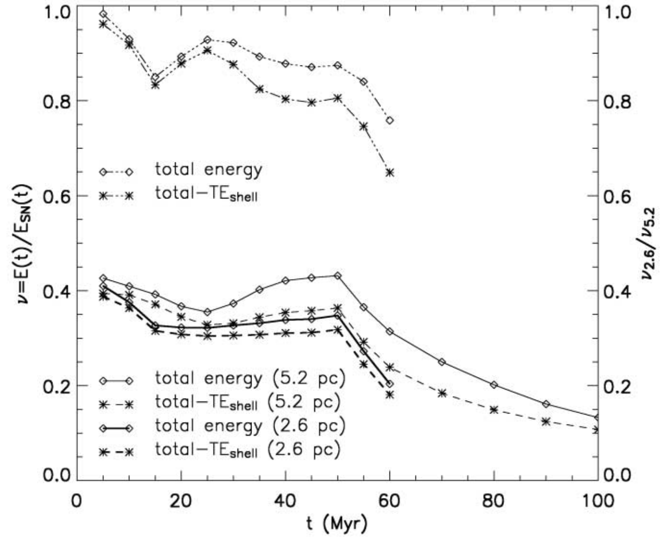

FIG. 11.—Resolution study of fractions of total injected energy remaining on the grid with $M = 5 \times 10^8\ M_\odot$ at $z = 8$, with $f_* = 0.01$. The main panel shows the total energy (*solid line with diamonds*) and the total energy excluding the thermal energy carried by swept-up gas (*dashed line with stars*) with standard resolution (5.2 pc: *thin lines*) and doubled resolution (2.6 pc: *thick lines*). The ratio of the results at the two resolutions is shown at the top of the figure. Note that the bubble with doubled resolution escapes the grid at $t = 60$ Myr.

We now crudely estimate whether turbulence driven by starburst bubbles in the very first dwarf galaxies could also delay and suppress the formation of subsequent dwarf galaxies with the same or larger mass $M_g > M_{\rm J}$. We can estimate how much turbulent energy a single dwarf starburst galaxy can supply to surrounding overdense regions with baryonic density ρ by dividing the escaping energy by the volume of the bubble at R_b:

$$v_{\rm rms} = \left(\frac{2\langle \zeta L_m t_f\rangle}{(4/3)\pi\rho R_b^3}\right)^{1/2}$$
$$\approx (40\ {\rm km\ s^{-1}})\left[\left(\frac{\zeta}{0.1}\right)\left(\frac{f_*}{0.01}\right)\right]^{1/2}$$
$$\times \left(\frac{\rho/\bar{\rho}}{5}\right)^{-1/2}\left(\frac{R_b}{5R_v}\right)^{-3/2}, \qquad (24)$$

where we used equation (7) with $t_f = 50$ Myr. This depends on the energy ejection efficiency ζ, the star formation efficiency f_*, and the halo virial radius $R_v = R_v(M_h, z)$ from equation (16). Note that the average density of a gravitationally bound object at turnaround $\rho/\bar{\rho} = 9\pi^2/16 \approx 5.6$ from the spherical collapse model. Based on our simulations, we estimate $v_{\rm rms} \approx 40$ km s^{-1} with $f_* = 0.01$ from galaxies with $v_c \lesssim 50$ km s^{-1}, assuming $\rho/\bar{\rho} = 5$ and $R_b = 5R_v$. The same level of turbulence could result from efficient star formation, $f_* \sim 0.05$, yielding $\zeta \approx 0.02$ in galaxies with $v_c \approx 100$ km s^{-1}. Recall that the kinetic energy of the wind is carried by the swept-up halo and intergalactic gas and is transformed to turbulence through dynamical instability. Therefore, equation (24) underestimates the amount of turbulence at the edge of the bubble but overestimates it within the bubble.

In order to delay and suppress cooling in halos with v_c, the turbulence with $v_{\rm rms} \approx v_c$ must be driven and maintained by repeated starbursts occurring on a dissipation timescale of the turbulence in equation (24):

$$t_{\rm cr} = R_{\rm vir}/v_{\rm rms} \approx 0.3\ {\rm Gyr}\left(\frac{v_{\rm rms}}{v_c}\right)^{-1}\left[\frac{(1+z)}{4}\right]^{-3/2}$$
$$< t_{\rm H}(z) \approx 1.9\ {\rm Gyr}\left[\frac{(1+z)}{4}\right]^{-3/2}. \qquad (25)$$

Note that some fraction of cooling in the halos with v_c can be suppressed by $v_{\rm rms} \approx v_c/2$, since the turbulent pressure delays the turnaround of gas from the Hubble flow.

The Press-Schechter mass function for our ΛCDM model predicts the mean separation of dwarf galaxies corresponding to 2 σ peaks to be $\sim 10\ R_v$, independent of mass and redshift, when they are assumed to reside in overdense filaments with $\rho/\bar{\rho} \approx 5$–$10$ (corresponding to a volume-filling factor of a few percent). This is likely to be an overestimate, since 2 σ peaks will be clustered. In addition, the mean separation of all the dwarf galaxies at a given epoch will be smaller, so we assume bubbles from these galaxies collide with other bubbles at $\sim 5\ R_v$ on average. Starburst bubbles are powerful enough to reach distances much greater than a few virial radii by $t = 50$–100 Myr in our models with $v_c \lesssim 50$ km s^{-1} and $f_* = 0.01$ and in all models with $f_* = 0.1$. Therefore, we can only expect these sorts of halos, which typically form from 1–2 σ peaks, to provide turbulence of the order of ~ 40 km s^{-1} to the IGM. Such starburst-driven turbulence may delay and suppress the cooling of the gas in future halo formation sites.

The turbulent Jeans mass (Chandrasekhar 1951) is

$$M_{{\rm J},t} \approx 2.4 \times 10^{10}\ M_\odot \left(\frac{1+z}{4}\right)^{-3/2}$$
$$\times \left[\left(\frac{c_s}{16\ {\rm km\ s^{-1}}}\right)^2 + \frac{1}{3}\left(\frac{v_{\rm rms}}{16\ {\rm km\ s^{-1}}}\right)^2\right]^{3/2}, \qquad (26)$$

where $c_s = 16$ km s^{-1} is the sound speed of the IGM with $T = 2 \times 10^4$ K. The Jeans mass is 5.4 times larger than the thermal Jeans mass alone for halos with $v_{\rm rms} = 40$ km s^{-1}, corresponding to $v_c \approx 120$ km s^{-1}.

This mechanism is analogous to the suppression of dwarf galaxies by UV background radiation (Bond et al. 1988; Meiksin 1994; Vedel et al. 1994; Thoul & Weinberg 1996; Navarro & Steinmetz 1997; Shapiro et al. 2004), except that the gas is energized by turbulent flows rather than thermal pressure due to ionizing radiation. Semianalytical studies of galaxy formation suggest that suppressing the fraction of gas that can cool and form stars below ∼10%–20% in halos with $v_c \approx 50$–100 km s^{-1} can reproduce the shape of the observed galaxy luminosity function (e.g., Cole et al. 1994).

Some cosmological simulations have demonstrated that the galactic outflows that they model, although not based on superbubble dynamics, can suppress the formation of dwarf galaxies by heating up the gas by shocks (Theuns et al. 2002) and by stripping the gas from the potentials by their momentum (baryonic stripping; Scannapieco et al. 2001). We agree that starburst-driven turbulent flows may play an important role in regulating the formation of galaxies, and so may be a key to the long-standing problems of overcooling and angular momentum losses in a CDM universe. It appears useful to model such starburst-driven turbulence in more detail in cosmological simulations, in order to address such questions.

In terms of the locally induced metallicity Z, the rms turbulent velocity is

$$v_{\rm rms} \approx (60 \text{ km s}^{-1}) \left(\frac{\zeta}{\xi_{\rm met}}\right)^{1/2} \left(\frac{Z}{10^{-2}\ Z_\odot}\right)^{1/2}. \quad (27)$$

The trend toward larger galaxy masses dominating metal ejection at later times (see Fig. 9) suggests that $v_{\rm rms}$ may increase with decreasing redshift. The values found for $v_{\rm rms}$ are comparable to the level of kinematic disturbance measured in C IV systems (Rauch et al. 2001a), suggesting that the metal deposition may have been recent in these systems, before the turbulence had time to dissipate. For a lower mean intergalactic metallicity of $Z = 0.001\ Z_\odot$, $v_{\rm rms} \approx 20$ km s^{-1}, which could result in significant broadening of the Lyα absorption systems and help account for the discrepancy between the predicted and measured line widths detected even in the optically thin systems (Meiksin et al. 2001). On the other hand, there would likely have been adequate time for the turbulence to dissipate by the time the winds could reach the underdense regions where the optically thin systems are expected to reside. Although the energy of the turbulence may be converted into heat as the turbulence dissipates, it is unclear how efficient this would be. Over a local Hubble time $t_{\rm H}(z)$, the energy associated with the turbulence, even if converted to heat, would also decay because of cosmological expansion. This is a topic that requires further exploration.

5.2. *Pressure Confinement of Bubbles*

All of the bubbles in our models are confined by external pressures if $f_* = 0.001$, while all escape to the IGM if $f_* = 0.1$. These results agree with our prediction in Figure 1 if the fraction of energy preserved in the bubbles $\nu \lesssim 0.2$. For a detailed analysis of how ram pressure affects the evolution of the bubbles, we choose models with $M_h = 5 \times 10^9\ M_\odot$ and $f_* = 0.01$ at $z = 3$, 5, and 8, in which the efficiency of metal and mass ejection and of energy transport decrease steadily as a function of redshift. We also try to constrain ν in equation (8) by comparing our results with Figure 1.

We plot in Figure 12 the initial total pressure distributions as a function of radius in these three halos. We examine the sum of thermal and ram pressure because some kinetic energy is converted to thermal energy in shocks owing to the artificial turnoff of cooling in the central regions, but the total energy is still conserved, since we do not solve for collisional cooling in the infall code (see § 3.1). We also plot the total pressure distributions of bubbles at 45° from the plane of the disks, measured at $t = 85$ Myr, for the halos at $z = 3$ and 8. The ram pressure is included only for the noncolored gas moving with positive radial velocities.

Figure 12 shows that the total pressure in the undisturbed halos in our models is a factor of 5 lower at $r \lesssim R_v$ than the ram pressure of the infalling halo gas calculated from equations (4) and (6) in § 2, but the difference is less than a factor of 2 outside R_v. Since pressure confinement mostly acts at $r \gtrsim R_v$ for powerful bubbles with $f_* \gtrsim 0.01$, we can reasonably compare our results with the prediction made in § 2. The external pressure increases as a function of redshift, consistent with the prediction from equation (4): $\rho v_{\rm in}^2 \propto (1+z)^4$.

Now we try to constrain the bubble energy fraction ν. All the bubbles in models with $f_* = 0.01$ expand beyond R_v by $t = 50$ Myr when the starbursts end, except along the planes of the galaxies, where the ISM offers the most resistance (Fig. 5*b*). The bubbles generally grow to $r = 2R_v$ by $t \approx 100$ Myr, leaving most of the ISM and the fragmented shells of swept-up halo gas behind. The halo pressure has already begun to confine the bubble at $z = 8$ by $t = 85$ Myr (Fig. 12). Only a small fraction of the original bubble energy remains at the swept-up shells in the form of kinetic energy. As a result, metal, mass, and energy feedback efficiencies are less than a few percent. Pressure confinement begins much later at $z = 5$, at $t \approx 150$ Myr, after the bubble grows beyond $2R_v$. Since we assume that the low-density IGM begins at $2R_v$, we compute moderately high ejection efficiencies of metals and halo mass of ∼0.3–0.4 in this case. The pressure on the bubble at $z = 3$ is more than an order of magnitude less than at $z = 8$ (Fig. 12), so it expands beyond $2R_v$ without any significant influence from the infall, expelling most of the metals and returning a large fraction of infalling gas into the IGM.

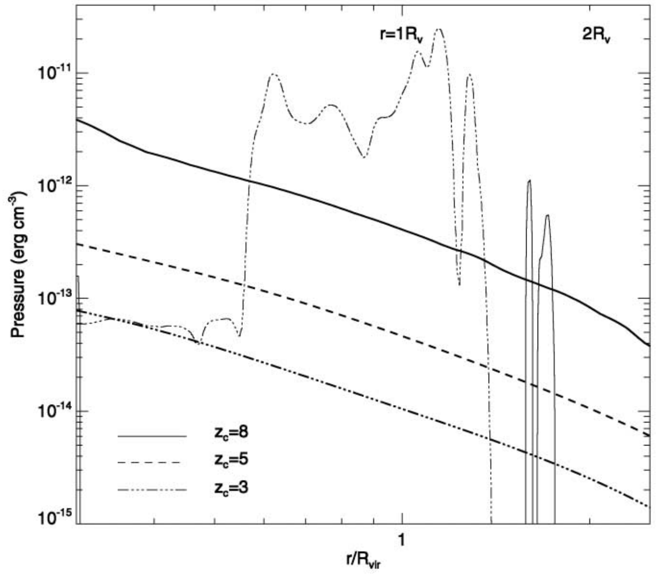

FIG. 12.—Initial pressure profiles (sum of thermal and ram pressure) for halos with $M_h = 5 \times 10^9\ M_\odot$ at $z = 8$ (*thick solid line*), 5 (*thick dashed line*), and 3 (*thick triple-dot–dashed line*) as a function of radius r normalized by virial radius R_v. We also plot pressure distributions of bubbles at 45° from the plane of the disks in the halos at $z = 8$ (*thin solid line*) and 3 (*thin triple-dot–dashed line*) at $t = 85$ Myr after the onset of starbursts with $f_* = 0.01$. The bubble at $z = 8$ has begun to be confined by external pressure, while the bubble at $z = 3$ freely expands to the IGM.

These halos fall just around the line of pressure confinement with $\nu f_* = 1 \times 10^{-3}$ in Figure 1. We compute ν in our models by summing the energy of interior gas with $c < 0.6$ and swept-up gas with positive velocity and dividing by $L_m t_f$. More than half of the injected energy has already been lost in these halos by $t = 50$ Myr. Loss occurs by radiative cooling in the swept-up shells and in the mixed gas after the shells fragment. It continues as time progresses and is larger at higher redshift. Our resolution study shows that the dissipation of bubble energy seen in our simulations is physical, not dominated by numerical diffusion (see Fig. 11).

We find the average energy fraction to be $\nu \sim 0.2$ between $t = 50$ and 100 Myr in the halos with $M_h = 5 \times 10^9\ M_\odot$ and $f_* = 0.01$ at $z = 3$ and 5, and to be $\nu < 0.2$ at $t = 50$ Myr and $\nu \lesssim 0.05$ by $t = 85$ Myr in the same halos at $z = 8$. Therefore, we have $\nu \approx 0.1$–0.2 from our simulations for $f_* = 0.01$, and so our results are consistent with the prediction made in Figure 1. We can also use equation (9) to define the confinement criterion in terms of virial temperature or circular velocity instead, finding that halos with $T_v \gtrsim 1.0 \times 10^5$ K or $v_c \gtrsim 52$ km s^{-1} will begin to confine a starburst with $f_* = 0.01$ and $\nu \approx 0.1$. On the other hand, ν increases more than a factor of 2 to $\nu \gtrsim 0.6$ in the same halos when $f_* = 0.1$. This is because the cooling time of the swept-up shells τ_s becomes larger than the dynamical time of the bubbles within $2R_v$, so the shocks remain adiabatic and the fragmentation of the shells is suppressed. Bubbles, even in galaxies with $v_c \sim 280$ km s^{-1}, cannot be stopped by ram pressure if $f_* = 0.1$ with $\nu \gtrsim 0.6$.

In summary, the ram pressure of the infalling halo gas strongly influences feedback efficiency in dwarf galaxies, although it is primarily determined by the strength of star formation. The analytic results of § 2 appear to offer a reliable guide to the importance of ram pressure.

5.3. *Fallback Timescales*

We compute the time for swept-up ISM and halo gas to cool and fall back to the center, which gives a minimum time before the next starburst. We define the accretion fraction as

$$\Upsilon(t) = M_4(R, t)/M_4(R_*, 0), \qquad (28)$$

where $M_4(R, t)$ is the gas mass with $T < 10^4$ K within radius R at time t, and R_* is the size of the galactic disk. Since we run our simulations for 200 Myr after the onset of starbursts or until the bubbles leave the grids, we first compute $\Upsilon(t)$ up to the end of the runs with $R = R_*$.

If most of the gas is bound to the potential at that time but has not yet fallen back to the center, we calculate $\Upsilon(t)$ for later times using a one-dimensional, ballistic approximation with $R = 0$. Bound gas parcels with $v < v_{\rm esc}$ are assumed to travel on radial, ballistic orbits in the potential, ignoring nonradial motions and acceleration of the accretion by cooling. We apply the approximation to gas within $2R_v$ at the time that feedback efficiencies are computed. This simple ballistic approximation was used by Zahnle & Mac Low (1995) to follow the ejecta of a typical Shoemaker-Levy 9 impact falling back onto Jupiter's atmosphere, and was found to give results consistent with observations. We also tested the validity of the method by computing the accretion fraction $\Upsilon(t)$ based on the ballistic approximation in a model in which we also compute $\Upsilon_{\rm sim}(t)$ directly in the simulations. The bottom panel of Figure 13 shows that they agree to within ~5%. We find similarly good agreement for other cases in which $\Upsilon_{\rm sim}(t)$ approaches unity so that we can make the comparison.

Figure 13 also shows the accretion fractions $\Upsilon(t)$ as a function of time for three halos with $M = 5 \times 10^9\ M_\odot$ at $z = 3$, 5, and 8, with $f_* = 0.01$ and 0.001. Because the ballistic model is only a one-dimensional approximation, it does not give exactly the same answer as the numerics at low values of Υ, as seen in Figure 13. We also define the fallback time τ_f as the time when $\Upsilon(\tau_f) = e^{-1}$, and give τ_f for all our model halos in Table 3. The bump in $\Upsilon(t)$ for the $z = 8$ model occurs when ISM material falls back to the center almost at the free-fall velocity, creating accretion shocks.

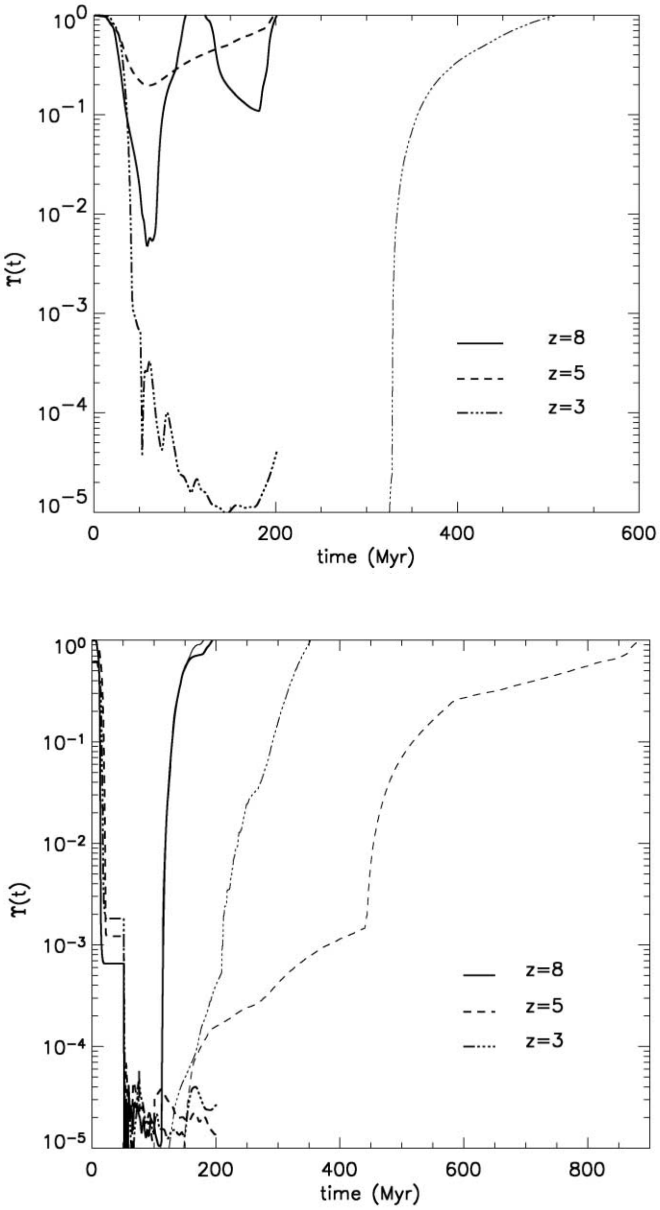

FIG. 13.—Accretion fraction $\Upsilon(t)$ for halos with $M_h = 5 \times 10^9\ M_\odot$ at $z = 3$ (*triple-dot–dashed lines*), 5 (*dashed lines*), and 8 (*solid lines*) with star formation efficiency $f_* = 0.001$ (*top*) and 0.01 (*bottom*). The accretion fractions computed from the simulations are plotted in thick lines and those computed based on the ballistic approximation are plotted in thin lines. In the bottom plot, the ballistic approximation is also compared with the simulation directly for the $z = 8$ model, showing no more than 5% deviation.

Since none of the mass escapes in models with $f_* = 0.001$, $\Upsilon(t)$ quickly approaches unity within $0.2t_{\rm H}(z)$. With $f_* = 0.01$, feedback is more efficient in halos at lower redshift, but the timescale for gas to fall back remains $\lesssim 0.4t_{\rm H}(z)$. This is rather significant in halos at $z = 3$ and 8 that have measured mass ejection efficiencies $\xi \approx 1$. Most disk gas appears tightly bound in galaxies with star formation efficiencies $f_* \lesssim 0.01$. In such galaxies, subsequent starbursts will occur in pre-enriched gas with a fraction $(1 - \xi_{\rm met})$ of the metals from previous starbursts, yielding

$$Z \approx 0.06\left(\frac{1 - \xi_{\rm met}}{0.5}\right)\left(\frac{f_*}{0.01}\right) Z_\odot. \qquad (29)$$

The presence of processed metals probably enhances star formation efficiency, which is the dominant factor influencing stellar feedback in our simulations. If the initial starbursts are very large, with $f_* = 0.1$, the mass in the halos is blown away and does not fall back within the local Hubble time $t_{\rm H}(z)$. Of course, real galaxies may never reach this star formation efficiency, as we discussed in § 4.

TABLE 3

Estimated Fallback Time τ_f

z (1)	M_h ($M_\odot$) (2)	τ_f			$t_{\rm H}$ (Myr) (6)
		$f_* = 0.001$ (Myr) (3)	$f_* = 0.01$ (Myr) (4)	$f_* = 0.1$ (Myr) (5)	
13	5×10^8	65	110	230	290
8	5×10^9	91	140	$\gg t_{\rm H}$	570
	5×10^8	127	160	$\gg t_{\rm H}$	570
5	5×10^{10}	116	280	$\gg t_{\rm H}$	1000
	5×10^9	109	320	$\gg t_{\rm H}$	1000
3	5×10^{10}	320	460	$\gg t_{\rm H}$	1900
	5×10^9	360	740	$\gg t_{\rm H}$	1900

Note.—Col. (1): Redshift. Col. (2): Halo mass. Cols. (3)–(5): Estimated fallback time such that $\Upsilon(\tau_f) = e^{-1}$. Col. (6): Hubble time at given redshift.

Our results suggest that it is difficult to keep most of the gas in a dwarf halo hot and diffuse and to prevent the central concentration of gas once a dense disklike object has formed. Star formation in small dwarf galaxies may occur in the form of repeating starbursts, although some other mechanism must explain the pauses longer than 10^9 yr between observed bursts of star formation.

If feedback is to solve the overcooling and angular momentum problems in the formation of massive galaxies, it must prevent the initial collapse and concentration of gas into dwarf galaxies in the halos of the massive galaxies. Once much of the gas in the massive halo has cooled to form dwarf galaxies, subsequent starbursts in the dwarf galaxies have great difficulty heating and expelling it permanently. The dwarf galaxies then lose angular momentum from dynamical friction against the parent dark halo. Feedback from dwarf galaxies may prevent gas in nearby dwarf halos from collapsing, however, leaving a reservoir of diffuse gas to build a massive galaxy without the baryons losing too much angular momentum through dynamical friction.

6. CONCLUSION

We study feedback from dwarf starburst galaxies with virial temperatures $T_v > 10^4$ K at high redshift by numerically modeling the interaction of superbubbles driven by repeated supernova explosions with the ram pressure from cosmological infall. We compute ejection efficiencies for mass, ξ, metals, $\xi_{\rm met}$, and energy, ζ, after the bubbles have expanded well beyond the virial radius, and estimate the timescale for disturbed gas to fall back and become available for subsequent starbursts. We have tried to consistently choose approximations that underestimate the effects of supernova feedback, so that our computations of the efficiency of mass, metal, and energy feedback and fallback time should be reasonably strong lower limits to the actual values. We now list our conclusions.

1. Ejection and transport efficiencies are primarily determined by the efficiency of star formation, f_*. With $f_* = 0.1$, nearly all the metals produced in the starburst escapes ($\xi_{\rm met} \approx 1$), most of the disk ISM and large parts of the infalling halo are blown away ($\xi > 1$), and accelerated halo gas carries the energy of the bursts out to the IGM ($\zeta > 0.5$). With $f_* = 0.01$, moderate to high feedback efficiencies are only observed in halos with $v_c \approx 30$–50 km s^{-1}. With $f_* = 0.001$, none of the metals, the mass, nor the energy can escape the potentials.

2. The ram pressure of infalling halo gas can suppress the growth of starburst bubbles and thus prevent the metal, mass, and energy feedback, unless $f_* \gtrsim 0.1$. The energy available to drive the bubble depends both on f_* and on the fraction of energy in the hot gas actually available to drive the bubble, ν. The minimum halo mass for ram pressure confinement with a given νf_* can be specified by a cutoff in virial temperature, T_v^*, or circular velocity, v_c^*, at any redshift (eq. [9]). Our prediction is consistent with the values of ν, $\xi_{\rm met}$, ξ, and ζ found in our simulations for a given f_*. With $\nu f_* = 1 \times 10^{-3}$, we can only expect high feedback efficiencies in halos with $T_v \lesssim T_v^* \approx 1 \times 10^5$ K and $v_c \lesssim v_c^* \approx 52$ km s^{-1}, above the limit for hydrogen line cooling and below the Jeans mass in the reheated IGM.

3. We find that small dwarf galaxies with $v_c \approx 30-50$ km s^{-1} at $z \lesssim 8$ are efficient in enriching the IGM with metals, yielding $\bar{Z} \gtrsim 10^{-3}$ $Z_\odot$ with $f_* = 0.01$. The early metal enrichment may be able to explain the absence of kinematic disturbance observed in low-density Lyα clouds. Larger dwarf galaxies with $v_c \approx 100$ km s^{-1} at $z = 3-5$ might enrich the IGM more effectively, yielding $\bar{Z} \approx 10^{-2}$ $Z_\odot$, because the efficient cooling expected in such halos may enable $f_* \gg 0.01$. The late metal enrichment is consistent with the high metallicities and large turbulent motions observed in high-density Lyα clouds. These galaxies form out of 1–2 σ peaks in our ΛCDM Gaussian density perturbation.

4. We expect mass ejection efficiencies $\xi \approx 0.3-1$ and energy transport efficiencies $\zeta \approx 0.1-0.3$ from the dwarf galaxies with $v_c \approx 30-50$ km s^{-1} with $f_* = 0.01$. However, most of the ISM remains bound unless $f_* = 0.1$. Instead, a large amount of infalling gas is turned around by the galactic wind and escapes the potential. This outflow may carry kinetic energy into the IGM, broadening Lyα absorption systems, and to other nearby halos to prevent gravitational collapse of the gas in them. We estimate that the ensemble of outflows may provide turbulent support with a typical $v_{\rm rms} \approx 20-40$ km s^{-1}. Further study of this multiscale problem is required to determine whether this mechanism of suppressing dwarf galaxy formation can solve the overcooling and angular momentum problems.

5. The timescale for swept-up mass to fall back to the center of a halo is short compared to the Hubble time, $\tau_f \lesssim 0.4 t_{\rm H}(z)$ if $f_* \lesssim 0.01$. We expect star formation efficiencies for subsequent starbursts to be larger than those of the initial starbursts that we studied, because ejected metals bound in the potentials will enhance gas cooling. Once gas in a halo cools to form a disklike object, it is difficult to blow away the disk gas.

We must mention the caveats to our study:

Our models assume an instantaneous starburst at the center of a galactic disk. This is obviously an oversimplification, and such instantaneous starbursts, especially with $f_* \gg 0.01$, are probably not realistic. We instead expect multiple OB associations or star clusters to form over a few hundred pc across the disk (e.g., Vacca 1996; Martin 1998). Each cluster will likely behave like our models, however, so the net effect will be greater than we compute, consistent with our attempt to present lower limits to the effects of stellar feedback. Given the dominant influence of the star formation efficiency on the importance of stellar feedback, a self-consistent, physically motivated modeling of star formation will be required to further our understanding.

We entirely neglected magnetic fields in this study. Magnetic fields can inhibit the formation of cold, dense shells and suppress the fragmentation of the shells, perhaps reducing or preventing the dissipation of the bubble energy through the fragmented shells. Thus, the fraction of energy preserved in the bubbles, ν, might be larger, giving higher feedback efficiencies in the dwarf galaxies that we modeled. On the other hand, magnetic pressure and tension might act to help confine the expanding bubbles (e.g., Tomisaka 1998), depending on the strength of the field.

Our models are not three-dimensional. This has consequences for two main reasons. First, we compute the Rayleigh-Taylor instability in fragmenting shells during blowout in two dimensions. This has the effect of increasing the size of the fragments (Mac Low et al. 1989) because only ringlike modes of the instability can form. In three dimensions, the instability takes on a spike and bubble form, with the spikes representing the dense fragments. This does not change the gross topology, since even in two dimensions the shell still overturns and the wind can escape. However, a detailed study of the fragment properties cannot be done. As we restrict ourselves to integrated quantities, however, this probably does not strongly affect our results. Certainly, the two models computed by Wada & Venkatesan (2003) in three dimensions appear to grossly agree with our results: a star formation efficiency of $f_* = 0.14$ in a galaxy with $10^7\ M_\odot$ of gas leads to metal escape, while with $f_* = 0.014$ the metals remain confined.

Second, our models assume a spherically symmetric gas infall and the presence of a well-formed, rotationally supported disk. It is also an oversimplification to compute metal, mass, and energy feedback efficiencies when the bubbles reach $R_s = 2R_v$. Realistically, a halo is embedded in the complicated weblike structures predicted by three-dimensional hydrodynamic simulations (e.g., Miralda-Escude et al. 1996; Zhang et al. 1998). Even inside its virial radius, gas accretion occurs along filaments and the accretion shock remains highly aspherical even after the protogalaxy has collapsed to less than a few times the virial radius, (Abel et al. 1998, 2000, 2002). In addition, a rotationally supported disk may not form before a significant amount of star formation occurs. We note, however, that a more dynamical, filamentary background will create funnels through which superbubbles and galactic winds can freely expand, potentially increasing the efficiency of metal ejection and energy transport.

Although these caveats identify important points requiring further investigation, none of them appear to invalidate our results, nor do they suggest that our lower limits are drastic underestimates of the actual effects of stellar feedback.

We thank T. Abel, M. Norman, J. Sommer-Larsen, V. Springel, and E. Tolstoy for useful discussions, and S. Glover, S. Kahn, and Z. Haiman for careful reading of the manuscript. We also thank B. Ciardi for providing useful data to us. A. F. was supported by the Beller Fellowship of the American Museum of Natural History. She thanks the Theoretical Astrophysics Center in Copenhagen for hospitality during work on this project. M.-M. M. L. was partly supported by NSF grants AST 99-85392 and AST 03-07854. A. F. acknowledges support from the RTN Network The Physics of the Intergalactic Medium, set up by the European Community under the contract HPRN-CT2000-00126 RG29185. A. M. thanks the University of Edinburgh Development Trust for support. Computations were performed on the SGI Origin 2000 machines of the Hayden Planetarium and of the National Center for Supercomputing Applications. We thank M. Norman and the Laboratory for Computational Astrophysics for use of ZEUS. This research made use of the Abstract Service of the NASA Astrophysics Data System.

REFERENCES

Abel, T., Anninos, P., Norman, M. L., & Zhang, Y. 1998, ApJ, 508, 518
Abel, T., Bryan, G., & Norman, M. L. 2000, ApJ, 540, 39
———. 2002, Science, 295, 93
Avila-Reese, V., & Vázquez-Semadeni, E. 2001, ApJ, 553, 645
Becker, H. R., et al. 2001, ApJ, 122, 2850
Bertschinger, E. 1985, ApJS, 58, 39
Bond, J. R., Cole, S., Efstathiou, G, & Kaiser, N. 1991, ApJ, 379, 440
Bond, J. R., Szalay, A. S., & Silk, J. 1988, ApJ, 324, 627
Bromm, V., Coppi, P. S., & Larson, R. B. 1999, ApJ, 527, L5
———. 2002, ApJ, 564, 23
Bromm, V., Ferrara, A., Coppi, P. S., & Larson, R. B. 2001, MNRAS, 328, 969
Castor, J., McCray, R., & Weaver, R. 1975, ApJ, 200, L107
Chandrasekhar, S. 1951, Proc. R. Soc. London A, 210, 26
Clarke, D. A., & Norman, M. 1994, ZEUS-3D User's Manual (NCSA TR015; Urbana: NCSA)
Cole, S., & Lacey, C. 1996, MNRAS, 281, 716
Cole, S., Aragon-Salamanca, A., Frenk, C. S., Navarro, J. F., & Zepf, S. E. 1994, MNRAS, 271, 781
Colella, P., & Woodward, P. R. 1984, J. Comput. Phys., 54, 174
Cowie, L. L., Songaila, A., Kim, T.-S., & Hu, E. M. 1995, AJ, 109, 1522
Dekel, A., & Silk, J. 1986, ApJ, 303, 39
D'Ercole, A., & Brighenti, F. 1999, MNRAS, 309, 941
De Young, D. S., & Heckman, T. M. 1994, ApJ, 431, 598
Djorgovski, S. G., Castro, S., Stern, D., & Mahabal, A. A. 2001, ApJ, 560, L5
Efstathiou, G. 1992, MNRAS, 256, 43
Ellison, S. L., Songaila, A., Schaye, J., & Pettini, M. 2000, AJ, 120, 1175
Elmegreen, B. G. E. 2000, ApJ, 530, 277
Ferrara, A., & Tolstoy, E. 2000, MNRAS, 313, 291
Fujita, A., Martin, C. L., Mac Low, M.-M., & Abel, T. 2003, ApJ, 599, 50
Gaetz, T. J., & Salpeter, E. E. 1983, ApJS, 52, 155
Gammie, C. F., & Ostriker, E. C. 1996, ApJ, 466, 814
Gerritsen, J. P. E., & Icke, V. 1997, A&A, 325, 972
Glover, S. C. O., & Brand, P. W. J. L. 2001, MNRAS, 321, 385
Gnedin, N. Y. 1998, MNRAS, 294, 407
Haiman, Z., Abel, T., & Rees, M. J. 2000, ApJ, 534, 11
Hultman, J., & Pharasyn, A. 1999, A&A, 347, 769
Kashlinsky, A., & Rees, M. J. 1983, MNRAS, 205, 955
Katz, N. 1992, ApJ, 391, 502
Katz, N., & Gunn, J. E. 1991, ApJ, 377, 365
Klessen, R. S., Heitsch, F., & Mac Low, M.-M. 2000, ApJ, 535, 887
Kogut, A., et al. 2003, ApJS, 148, 161
Kompaneets, A. S. 1960, Sov. Phys. Dokl., 5, 46
Kudritzki, R. P. 2002, ApJ, 577, 389
Larson, R. B. 1974, MNRAS, 169, 229
———. 1988, MNRAS, 301, 569
Leitherer, C., et al. 1999, ApJS, 123, 3
Lockman, F. J., Hobbs, L. M., & Shull, J. M. 1986, ApJ, 301, 380
Mac Low, M.-M. 1999, ApJ, 524, 169
Mac Low, M.-M., & Ferrara, A. 1999, ApJ, 513, 142 (MF99)
Mac Low, M.-M., & McCray, R. 1988, ApJ, 324, 776
Mac Low, M.-M., McCray, R., & Norman, M. L. 1989, ApJ, 337, 141
Mac Low, M.-M., & Shull, J. M. 1986, ApJ, 302, 585
Madau, P., Ferrara, A., & Rees, M. J. 2001, ApJ, 555, 92
Martin, C. L. 1998, ApJ, 506, 222
Mathews, W. G., & Baker, F. C. 1971, ApJ, 170, 241
McCray, R., & Kafatos, M. 1987, ApJ, 317, 190
Meiksin, A. 1994, ApJ, 431, 109
Meiksin, A., Bryan, G., & Machacek, M. 2001, MNRAS, 327, 296
Miralda-Escude, J., Cen, R., Ostriker, J. P., & Rauch, M. 1996, ApJ, 471, 582
Mo, H. J., Mao, S., & White, S. D. M. 1998, MNRAS, 295, 319
Mori, M., Ferrara, A., & Madau, P. 2002, ApJ, 571, 40
Nakamura, F., & Umemura, M. 1999, ApJ, 515, 239
———. 2001, ApJ, 548, 19
Navarro, J. F., & Benz, W. 1991, ApJ, 380, 320

Navarro, J. F., & Steinmetz, M. 1997, ApJ, 478, 13
Navarro, J. F., & White, S. D. M. 1993, MNRAS, 265, 271
———. 1994, MNRAS, 267, 401
Neeser, M. J., Sackett, P. D., De Marchi, G., & Paresce, F. 2002, A&A, 383, 472
Oh, S. P., & Haiman, Z. 2002, ApJ, 569, 558
———. 2003, MNRAS, 346, 456
Omukai, K., & Nishi, R. 1999, ApJ, 518, 64
Press, W. H., & Schechter, P. 1974, ApJ, 187, 425
Rauch, M. 1998, ARA&A, 36, 267
———. 2002, ASP Conf. Ser. 254, Extragalactic Gas at Low Redshift, ed. J. Mulchaey & J. Stocke (San Francisco: ASP), 140
Rauch, M., Sargent, W. L. W., & Barlow, T. A. 2001a, ApJ, 554, 823
Rauch, M., Sargent, W. L. W., Barlow, T. A., & Carswell, R. F. 2001b, ApJ, 562, 76
Saito, M. 1979, PASJ, 31, 193
Salpeter, E. E. 1955, ApJ, 121, 161
Sargent, W. L. W., Young, P. J., Boksenberg, A., & Tytler, D. 1980, ApJS, 42, 41
Scannapieco, E., Ferrara, A., & Madau, P. 2002, ApJ, 574, 590
Scannapieco, E., Thacker, R. J., & Davis, M. 2001, ApJ, 557, 605
Sedov, L. I. 1959, Similarity and Dimensional Methods in Mechanics (New York: Academic)
Shapiro, P. R., Iliev, I. T., & Raga, A. C. 2004, MNRAS, 348, 753
Shapiro, P. R., & Kang, H. 1987, ApJ, 318, 32
Silich, S. A., & Tenorio-Tagle, G. 1998, MNRAS, 299, 249
Sommer-Larsen, J., Götz, M., & Portinari, L. 2002, Ap&SS, 281, 519
Songaila, A. 2001, ApJ, 561, L153
Songaila, A., & Cowie, L. L. 1996, AJ, 112, 335
Spergel, D., et al. 2003, ApJS, 148, 175
Spitzer, L., Jr. 1978, Physical Processes in the Interstellar Medium (New York: Wiley)
Springel, V., & Hernquist, L. 2003, MNRAS, 339, 289
Stone, J. M., & Norman, M. L. 1992, ApJS, 80, 753
Sutherland, R. S., & Dopita, M. A. 1993, ApJS, 88, 253
Tegmark, M., Silk, J., Rees, M. J., Blanchard, A., Abel, T., & Palla, F. 1997, ApJ, 474, 1
Thacker, R. J., & Couchman, H. M. P. 2001, ApJ, 555, L17
Thacker, R. J., Scannapieco, E., & Davis, M. 2002, ApJ, 581, 836
Theuns, T., Matteo, V., Scott, K., Schaye, J., Carswell, R. F., & Tzanavaris, P. 2002, ApJ, 578, L5
Thoul, A. A., & Weinberg, D. H. 1996, ApJ, 465, 608
Tomisaka, K. 1998, MNRAS, 298, 797
Tomisaka, K., & Ikeuchi, S. 1986, PASJ, 38, 697
Vacca, W. D. 1996, in The Interplay Between Massive Star Formation, the ISM, and Galaxy Evolution, ed. D. Kunth et al. (Paris: Editions Frontières), 321
van Leer, B. 1977, J. Comput. Phys., 23, 276
van Zee, L., Skillman, E. D., & Salzer, J. J. 1998, AJ, 116, 1186
Vedel, H., Hellsten, U., & Sommer-Larsen, J. 1994, MNRAS, 271, 273
Wada, K., & Venkatesan, A. 2003, ApJ, 591, 38
Weaver, R., McCray., R., Castor, J., Shapiro, P., & Moore, R. 1977, ApJ, 218, 377
White, S. D. M., & Frenk, C. S. 1991, ApJ, 379, 52
White, S. D. M., & Rees, M. J. 1978, MNRAS, 183, 341
Yabe, T., & Xiao, F. 1993, J. Phys. Soc. Japan, 62, 2537
Yepes, G., Kates, R., Khokhlov, A., & Klypin, A. 1997, MNRAS, 284, 235
Zahnle, K., & Mac Low M.-M. 1995, J. Geophys. Res., 100, 16885
Zhang, Y., Meiksin, A., Anninos, P., & Norman, M. L. 1998, ApJ, 495, 63